Journal of Nondestructive Evaluation (2024) 43:45
https://doi.org/10.1007/s10921-023-01043-8

Air-Coupled Broadband Impact-Echo Actuation Using Supersonic Jet Flow

Christoph Strangfeld[1] · **Bjarne Grotelüschen**[1] · **Benjamin Bühling**[2]

Received: 28 August 2023 / Accepted: 25 December 2023

Abstract

The impact-echo method (IE) is a non-destructive testing method commonly used in civil engineering. We propose a completely new approach for air-coupled actuation based on supersonic jet flow. The impinging jet sound generates continuously high sound pressures with a broad frequency bandwidth. This novel concept of utilising aeroacoustic sound for air-coupled IE was evaluated on two concrete specimens and validated using a classical IE device with physical contact. The results show a high agreement with the expected frequencies. Delaminations are correctly detected in depth and size. This proves the high reliability of air-coupled IE based on supersonic jet flow.

Graphic abstract

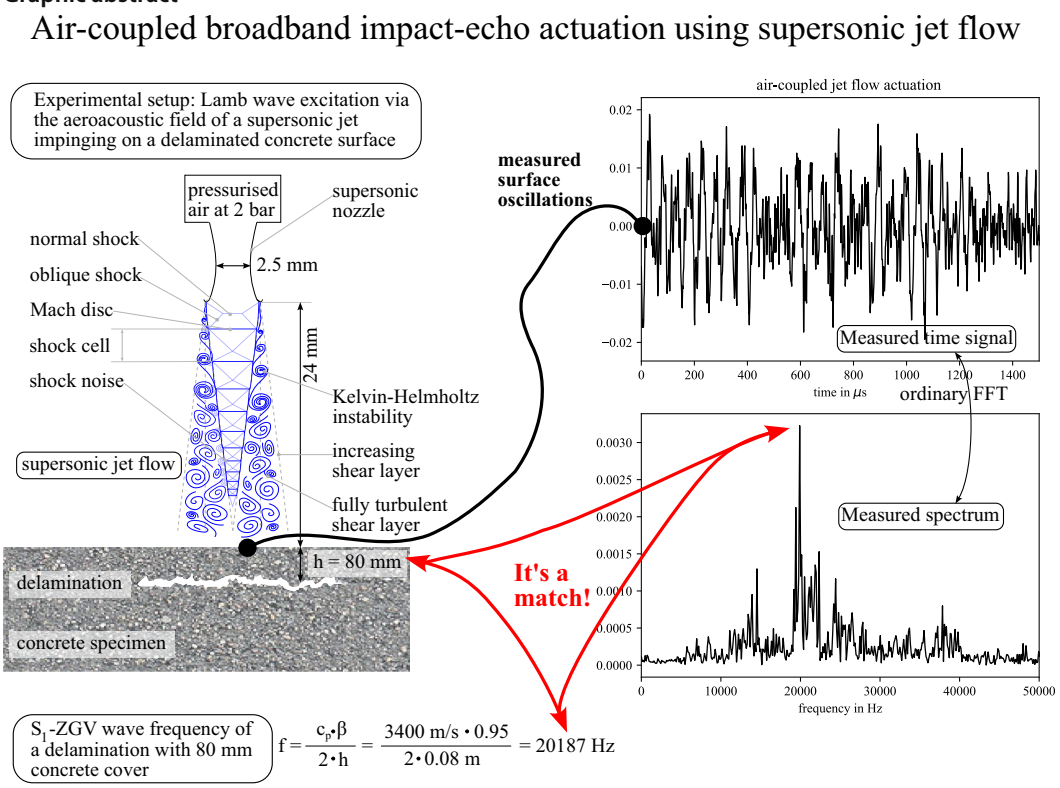

Keywords Air-coupled impact-echo · Impact-echo actuation · Building materials · Delamination · Aeroacoustic actuation · Impinging jet

Extended author information available on the last page of the article

Published online: 13 April 2024

1 Introduction

The transport infrastructure of modern industrialised countries will face several challenges in the future. With increasing economic activity, total freight transport has increased in recent decades and is expected to continue to rise, for example truck freight transport in the EU by 44 % by 2050 [1]. This puts even more loads on road and rail structures. In several countries, large parts of the current transport infrastructure were built in the 1950 s to 1970 s [2]. After this long time in service, several structures show serious degradations or might reach their expected lifespan. These two aspects lead to a global investment in transport infrastructure of around $2 trillion per year by 2040 [3]. Moreover, modern industry has changed in recent decades from warehousing to just-in-time delivery. A modern infrastructure needs to be robust and reliable to avoid traffic congestion, detours [4], and, ultimately, production downtime. In addition, climate goals have been set that include the direct emissions of CO_2 from traffic and transport, as well as indirect CO_2 emissions generated by constructing and maintaining the current transport infrastructure.

An ageing transport infrastructure is facing increased loads, while degradations of entire structures is occuring at the same time. This affects single components or can occur locally inside the material. Most transport infrastructure is made of reinforced concrete and shows different types of degradation mechanisms, such as corrosion [5], carbonation [6], alkali-silica-reaction [7–9], delayed ettringite formation [10]. In case of corrosion, the volume of the corroded reinforcement expands and generates an internal compressive force. This may lead to a debonding of the concrete cover along the first layer of reinforcement. If this occurs over larger areas, large cracks oriented parallel to the concrete surface appear in the depth of the first layer of rebars; in practice mostly in a depth of 3 cm to 8 cm corresponding to the concrete cover. In the following, we speak here delamination, i.e. an almost two-dimensional crack area with a spatial extension several times larger than the concrete cover. This degradation is accompanied by a reduction in load-bearing capacity, leads to accelerated corrosion of the neighbouring areas and causes a significant reduction in serviceability lift and safety. Other construction technologies such as shotcrete or additive manufacturing bear the inherent risk of delamination between layers. Structures made with shotcrete lose significant structural integrity when delamination of areas occurs. A test method that is applicable while the structure is still in a visco-elastic state would be very useful to enable realtime counter-measures.

If not detected by non-destructive testing (NDT), delaminations lead to concrete spalling. This is a serious and dangerous situation for bridge decks and tunnel linings, which may damage transport vehicles and lead to sudden closure of these crucial transport infrastructure objects. Other materials are also affected by spalling. Asphalt is generally a layer system, consisting of a base layer and a cover layer, the latter is usually between 2 cm to 6 cm thick. Delamination between the two layers above a certain spatial extend leads to spalling of the cover layer, commonly known as potholes. A combination of concrete and asphalt is widely used for bridge decks, for example. The supporting reinforced concrete structure is covered with an asphalt layer, which can also spall [11, 12]. In high-speed railway infrastructure, solid track structures are widely employed. Typically, pre-stressed concrete track slabs, with a thickness of approximately 20 cm are used, which are connected to the base concrete roadbed using either asphalt or a cement-asphalt mortar as an adhesive [13]. However, it is crucial to address the potential issue of debonding between these two layers, as this poses a significant risk of displacing the entire rail track.

To enhance the reliability and safety of transport infrastructure, it is highly desirable to detect delaminations at an early stage. To address this, various non-destructive testing (NDT) methods have been employed to tackle the issue. In most cases, access to the concrete structure is limited to one side, such as tunnel walls. Therefore, we only discuss methods that measure in reflection mode. As an optical method, thermography is able to detect delamination due to reduced heat transfer in the affected area [14]. With the more advanced impulse-thermography, even the depth of the delamination can be estimated if the thermal properties of the material are known [15]. Thermal waves penetrate the material only slowly, making large-scale on-site measurements less economical. Still, this method is an outstanding tool for the validation of test specimens in the laboratory. Electromagnetic methods such as impulse radar need a contrast in permittivity. This can only work for water-saturated cracks and delaminations. In the hygroscopic moisture range, cracks of small width do not generate enough signal contrast and the probability of detection is drastically reduced [16, 17].

Other common methods are based on using elastic waves. Sounding, an established and still common method, uses construction hammers or steel chain drags as impactors [18]. With a relatively high mass of the impact body, only frequencies in the Hz range or lower kHz range are generated. At these frequencies, only flexural vibrations of the plate-like structure are excited and their detection highly relies on the delamination's geometry, the mechanical bearing conditions at its boundaries and the wave-number of this mode [19]. Consequently, smaller or deeper delaminations pose challenges for detection. Furthermore, highly trained personnel are required as sensing is performed directly with the human ear or with a shielded microphone that transmits the signal directly to a headphone [20]. An area scan of around 200 m^2 per hour could be realised. Noise cancelling techniques were also used to support the personnel [21]. Already

in 1977, a semi-automatic sounding trolley was developed that was equipped with knocking steel wheels [22]. Today, multi-channel systems based on six tyre chains allow a driving speed of up to 45 km/h during measurement [23]. A 12-channel acoustic cart is also used to scan bridge decks at up to 20 km/h [24]. In the future, the probability of detection could be significantly increased by the use of artificial intelligence [25]. A new approach for non-destructive corrosion measurements of rebars is the used of strong electromagnetic waves. The excitation coils generate vibrations of the rebars and the surrounding concrete [26, 27]. In future, this approach can be used to excite flexural modes of the reinforced concrete to perform sounding measurements. However, it is not known which flexural mode is excited, so the data evaluation remains arbitrary to a certain extend.

A better approach is a time-of-flight measurement based on pulse-echo ultrasound. An elastic wave with ultrasound frequencies is generated by a surface-coupled transmitter and penetrates the material. The emitted elastic wave is reflected at the back wall of the structure and travels back to the top surface. This reflected wave is recorded by the transmitter to determine the time-of-flight. The ultrasound transmitter must have a small acoustic aperture to avoid near field interferences, as delaminations can be close to the surface, e.g., 2 cm. This limitation hinders the utilisation of modern ultrasound array systems consisting of 12 or more synchronised transducers, or requires advanced data processing tools such as reverse time migration [28] or full waveform inversion [29]. Furthermore, the smaller the material thickness, the shorter the time-of-flight. This can lead to difficulties in sensing the echo signal, as it might interfere with not-subsided surface waves from the initial actuation. Therefore, a long-lasting measurement signal is preferable. This is the great advantage of the impact-echo (IE) method, which is also based on elastic waves [30]. This frequency-based approach uses small steel spheres as impactors to generate a IE wave (sometimes also named Lamb wave) on the plate-like structure above the delamination [31, 32]. Depending on the material properties, it is possible to measure 10 to 30 full periods, greatly simplifying data recording. The excited IE wave is also known as a plate thickness vibration and depends only on the plate thickness and the wave velocity. Thus, even simple FFT (Fast Fourier Transformation) approaches are sufficient for data analysis, which makes the data processing very robust. In the following, we focus on the IE method, as it represents a compromise between a sufficient probability of detection, a tolerable complexity of measurement procedure and the corresponding data processing.

In the first laboratory studies, surface-mounted accelerometers were used to record the surface displacement caused by the IE wave [11, 33–35], resulting in a slow measurement speed because of the sensor positioning. Consequently, much effort was put into contact-free sensing with single microphones [36–38] or microphone arrays [39]. To further improve the signal-to-noise ratio, parabolic focusing reflectors were positioned above the impact point to redirect a large portion of the spherical wave into the focal point where the microphone was placed [40]. Laser vibrometers are also applicable for sensing, but they are less robust and often too expensive [41]. To further increase the measurement speed, the impact of the steel sphere was triggered with a small motor [42, 43]. Contact-free sensing and automatised actuation were combined to develop hand-operated trollies to measure at walking speed [39, 44]. New approaches were developed using IE wave phase velocity for two-dimensional mapping of large concrete plates, covering several square meters [45]. The effectiveness of IE has been demonstrated in practical studies [20, 46] and validated through numerical simulations [47]. Moreover, internationally accepted standards have been developed [48, 49] highlighting the widespread acceptance of IE as a non-destructive testing method in civil engineering, particularly for assessing transport infrastructure.

The authors of this paper favour air-coupled actuation. As long as physical contact of steel balls is required, this measurement method does not have a suitable measurement speed and hinders the development of full automation or multi-channel/ array systems. The use of falling water droplets or ice spheres instead of steel balls has also been tested [50, 51]. Although the impactor material, i.e. water, can remain, it is still a physical and non-continuous contact to the surfaces, which limits the repetition rate of actuation. A similar approach is the use of a water jet disintegrating into individual droplets before hitting the concrete surface. Nevertheless, only flexural modes are as the generated impact frequencies are mainly below 1 kHz [52].

Another real air-coupled approach is to use a high energy laser to generate a plasma on the concrete surface [53]. The laser technique might not be robust and easy enough to handle for the construction site. Furthermore, the required frequencies were excited with insufficient energy [53]. Another air-coupled approach is the use of a shock tube for producing shock waves [54]. Experiments have demonstrated the applicability of shock tubes, but the measurement speed is very low due to the reloading of the shock tube. An electric spark sources has also been used for air-coupled actuation, but the heavy weight and the high energy required render this approach impractical for the construction site [55].

An optimal air-coupled IE actuator has to fulfil several specifications that result from the conditions on a construction site. It must be robust for working in dusty, dirty or foggy conditions. The actuation should run continuously to enable continuous data acquisition as well. This would drastically accelerate measurement speed, at least to walking speed or even faster. Rough or curved surfaces should be measurable. In tunnels or bridge boxes, energy supply and physical access are limited. Thus, the overall system should be light enough

to be carried by one person. The energy consumption should be so low that an external energy supply is not required. The actuator itself should be a small and light handheld device to enable manual scanning of vertical or overhanging structures even for hours. Finally, the technique should be inexpensive enough to allow the setting up of multi-channel and array systems, i.e., to cover the investigation of an entire pavement lane. By the best knowledge of the authors, an air-coupled IE actuator fulfilling all these requirements does not yet exist.

Our hypothesis in this paper is the following: Ordinary subsonic or supersonic air jets are able to generate continuously a broadband signal with sufficient sound pressure amplitude to excite IE waves at frequencies usable for IE measurements in civil engineering.

As this fluidic approach is completely new, the underlying fluid mechanics are discussed in more detail, including screeching and impingement sound. These aeroacoustic phenomena generate sound at very high pressure amplitudes. In almost all technical applications, this sound is considered as unwanted noise that needs to be attenuated or, in the best case, eliminated. We pursue the opposite way of thinking. Aeroacoustic "noise" of air jets is considered and used as a wanted acoustic actuation signal. Based on this novel approach, we describe the measurement setup and the concrete specimens used for validation. For experimental validation, we compare this new method with traditional and commercially available IE devices based on physical contact.

2 Theory

2.1 The Impact-Echo Method

The IE method was mainly developed by Sansalone and Carino in the mid and late 1980 s [11, 33–35]. The main idea is that a broadband impulse is generated and a plate-like structure begins to vibrate. For this purpose, a unit impulse, also known as Dirac impulse, would be ideal as it contains all frequencies. The resulting standing wave, i.e. the dominant frequency of the elastic plates, is also known as IE wave [56]. Thereby, the IE method corresponds to the zero point of the group velocity of the first order symmetrical S_1-ZGV wave of a free plate [57–61]. They can be detected as surface displacement. The waveform follows a sinusoidal function with an exponential decrease in amplitude [33]. The great advantage of this mode is that it depends only on the plate thickness and the wave speed, i.e., it is independent of the lateral dimension, geometry, or bearing conditions of the plate-like structures. This simplifies the data evaluation to the following ordinary equation:

$$h = \frac{c_p \beta}{2 f} \tag{1}$$

Here h in m represents the thickness of the plate structure and c_p in ms^{-1} is the pressure wave velocity of the considered material. β is a correction factor that depends on the material's Poisson's ratio and ranges from 0.945 to 0.975 [48, 60]. The last parameter f in s^{-1} is the standing wave frequency of the plate and can be measured by the displacement of the surface in the vicinity of the impact point. In experiments, this can be done by different devices, e.g. accelerometers, single microphones or microphone arrays, laser vibrometers. For data processing, common FFT approaches are mostly sufficient to extract the S_1-ZGV mode frequency from the recording. More advanced approaches such as wavelet transformation can increase the signal-to-noise ratio [62].

This study focuses on an air-coupled actuation for the IE method. Hence, the actuation itself is discussed in more detail below. In the beginning of IE, small steel spheres falling onto the concrete surface were used as actuators/ impactors. Later, to avoid rebounds, handheld sticks with a small steel sphere at one end were used, which is still common today. The sphere's weight varies between 0.5 g and 20 g, or expressed in diameter between 5 mm to 15 mm respectively [37]. The higher the weight, the more energy is transferred into the material. On the other hand, the increasing weight also increases the contact time [32]. The longer the contact time, the lower the frequencies that can be excited [31]. This also limits the maximum and minimum detection range. The latter is relevant for shallow delaminations and amounts to 14 mm with a sphere diameter of 2 mm [62]. However, the impact should be as powerful and sudden as possible to resemble a unit pulse. This would generate a maximum bandwidth to excite the S_1-ZGV wave of a free plate. When thick concrete structures with shallow delaminations are evaluated, the limited bandwidth of the steel sphere becomes challenging. One sphere might not be sufficient to excite the S_1-ZGV mode with sufficient energy of the shallow delamination and of the thick concrete slab concurrently. Therefore, experiments with shallow delaminations are often carried out twice at every measurement point, including a big sphere for the bottom structure and a small sphere for the shallow delaminations. As the contact time of physical contact is the limiting factor [31], this effect is analogous to other impactors such as ice spheres or water droplets [50, 51]. On the other hand, the actuation with laser ablation relies on the laser pulse length, which for most lasers is in the range of picoseconds or a few nanoseconds [53]. Although the thermoacoustic wave can persist in the generated plasma on longer time scales, frequencies above 50 kHz are the most excited and might dominate the spectrum [53]. This could inhibit laser-excited IE measurements on thick structures.

In transport infrastructure, however, most components are not thicker than 40 cm, while the lower limit for the minimum delamination depth is generally 2 cm. Based on a wave speed of 4000 ms^{-1}, this would lead to a frequency range between

5 kHz and 100 kHz. Within this "ideal" bandwidth, the excitation amplitude should be constant to avoid distortion in the received frequency spectrum.

2.2 Screeching of Supersonic Jets

Our hypothesis is that the required broadband actuation signal can be excited continuously by a fluidic jet without physical contact to the surface. To reduce complexity, in the following we consider only isothermal, single-flow jets exiting in steady state through a circular cross-section at the nozzle outlet into calm air. Depending on the nozzle pressure ratio (NPR), defined as supply pressure at the inlet and ambient pressure at the outlet, the exit velocity can be in the subsonic or supersonic range. In both cases, a shear layer forms between the high velocity jet and the calm air, as indicated in Fig. 1a. The velocity profile of this shear layer possesses an inflation point that leads to a natural, self-excited flow instability, the so-called Kelvin-Helmholtz instability [63, 64]. Small-scale vortices are generated there at high turbulence levels [65]. Downstream, the shear/mixing layer thickens, reducing the diameter of the jet's potential core. The latter is the "undisturbed" region where the velocity profile is not affected by the shear layer, as depicted in Fig. 1a. However, the emitted vortices within the shear layer, often called fine-scale turbulence, generate broadband sound [66]. Already at subsonic speed, this sound can reach significant sound pressure levels [67]. Therefore, a lot of research focuses on the attenuation or elimination of this shear layer sound, which has always been considered as unwanted noise. Although the aeroacoustic noise of these flow types has been intensively studied for more than a century [68], not all underlying flow mechanics are fully understood. For example, far-field jet noise has significant intermittent aspects that are not fully captured by current models [69], probably due to the highly turbulent flow. However, supersonic jets generate much higher sound pressure levels than subsonic jets, which is advantageous for IE actuation. Therefore, we will only discuss supersonic jet flow in more detail in the following.

With increasing NPR, the emitted flow speed increases and reaches supersonic velocities. In this case, the downstream flow field changes dramatically as shown in Fig. 1b. Furthermore, the aeroacoustic sound pressure increases significantly. These acoustic waves can induce vibrations in the surrounding structure, surface erosion in the nozzle or reduced thrust efficiency of the jet engine. Not surprisingly, most of the research is motivated by military applications such as supersonic flight manoeuvres, supersonic missiles, or the sound reduction of supersonic jet engines [70]. The latter is also highly relevant for civil aircrafts [71]. In general, one can distinguish between over-expanded and under-expanded nozzles. For our application, this distinction is of minor relevance. In all cases, however, the jet velocity becomes zero in the very far field. This transition from supersonic to subsonic velocities involves the formation of plane normal sonic shocks (Mach discs), oblique shocks, as well as compression and expansion fans. Depending on the ambient conditions, this shock wave pattern can repeat up to ten times before the growing mixing layers merge and close the potential core and envelop the supersonic jet as indicated in Fig. 1b. In our application, the supersonic jet is used as an acoustic actuator. Therefore, the flow field is of minor interest and will not be considered further.

The emitted shock wave pattern generates two additional mechanisms for sound generation, namely screeching and broadband shock-associated noise [66, 72, 73]. Combined with the turbulent mixing noise of the shear layer, already discussed for subsonic jets, these three flow components interact with each other and generate impressively high sound pressure amplitudes, as shown in Fig. 2. As this represents the source of our newly developed IE actuator, we briefly discuss the aeroacoustic field. The first theoretical and experimental studies of choked jet noise are performed by Powell in the early 1950 s [74]. Several holistic reviews describe the evolution of this research topic [66, 72, 73, 75].

The three noise-generating components have very individual, directional characteristics [66]. In the downstream direction, the turbulent shear layer noise is most dominant [66]. The shock pattern also generates a broadband noise, but at higher frequencies compared to the shear layer. Furthermore, this radiated shock-associated sound is more intense in the upstream direction [66]. Between the two broadband frequency areas, the third sound component is emitted, the screeching tone [72]. As shown in Fig. 2, this is a very distinct peak in the spectrum whose amplitude is often more than 10 dB higher than the broadband noise intensity. The fundamental mode of this tone radiates mainly in the upstream direction for circular jets [66]. Higher harmonics or different types of modes, such as azimuthal, helical or toroidal modes could be generated and dominate the aeroacoustic field with their own individual radiation characteristics, depending on nozzle geometry, jet temperature, NPR, and Mach number [66, 76]. This can lead to a frequency staging of the screeching tone, as different waven numbers are excited [77]. In general, screeching tone amplitudes decrease with increasing jet temperature [72]. As shock-associated screeching radiates at least partially upstream, the associated acoustic pressure waves are capable to reach the nozzle exit/lips (see Fig. 1b). At this point, the shear layer is formed. This amplifies the arising Kelvin-Helmholtz instabilities directly at their origin [77]. Then these amplified coherent structures travel downstream and undergo transition towards a fully turbulent shear layer [78]. Although turbulent, the original pattern of the coherent structure is still present in the shear layer, as demonstrated by the triple decomposition analyses [79, 80]. However, the downstream travelling shear layer, including

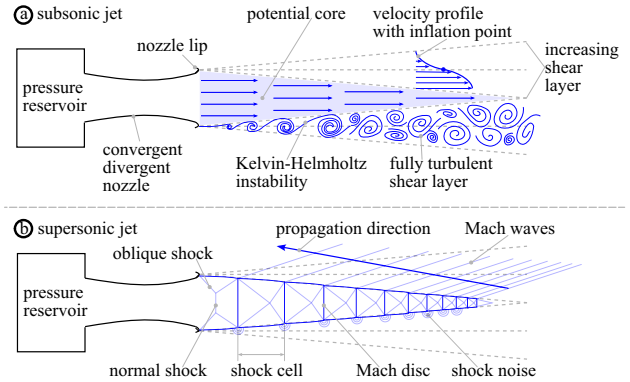

Fig. 1 Schematic of the flow field of a free jet entering calm air. **a** Subsonic jet flow: The inflation point of the velocity profile leads to the formation of Kelvin-Helmholtz instabilities and an increasing shear layer; **b** Underexpanded supersonic jet flow: the supersonic shock wave train is surrounded by the subsonic shear layer where Mach waves are generated

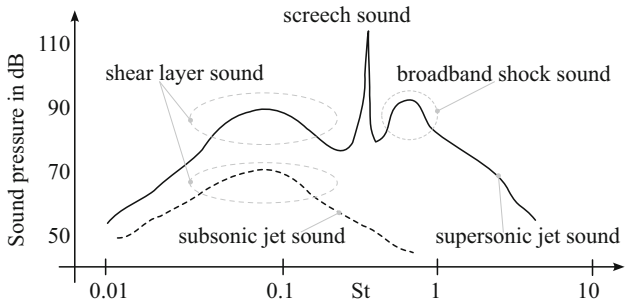

Fig. 2 Schematic of the emitted aeroacoustics of a free jet. **a** subsonic jet flow; **b** supersonic jet flow. This schematic is an ensemble of [66, 70, 72, 75, 77, 81]

its small oscillations, interacts with the shock waves. This can lead to a small spatial oscillation of the shock wave position, called the shock wave pattern [73]. In most publications, this shock wave pattern is considered to be the source for screeching tone generation. The upstream travelling acoustic pressure waves of the shock waves amplify the coherent structures in the shear layer, i.e. Kelvin-Helmholtz instability. These amplified coherent structures might amplify the shock wave pattern, which increases the acoustic pressure wave amplitude [66, 73]. This self-sustaining feedback loop is also the reason why supersonic jets generate much stronger shear layer noise compared to subsonic jets, because they are amplified directly at their origin. Furthermore, the interaction of the downstream travelling turbulence structures of the jet with the shock cell structure is thought to generate the high amplitude broadband shock-associated noise [73]. These large-scale turbulence structures, together with the radiated Mach waves, dominate the aeroacoustic field compared to the fine-scale turbulence structures of the shear layer [66]. Therefore, supersonic jets are considered to be very powerful high-amplitude broadband noise generators which run continuously.

Figure 2 shows a schematic representation of the sound pressure spectrum for a subsonic and supersonic jet. Due to the self-similarity of jets, we can use dimensionless frequencies based on the real frequency f, the nozzle exit diameter D in m and the jet velocity U in ms^{-1}. This results in the dimensionless Strouhal number $St = \frac{fD}{U}$. Since both jets form a shear layer, both sound spectra show increased broadband sound pressures around $St = 0.1$. Depending on NPR and temperature, this peak can be located between $0.2 > St < 0.7$ [81] However, in most applications it is around $St = 0.3$, but also depends slightly on the fundamental instability mode [66, 73]. Due to this interaction, the shear layer sound of a supersonic jet is significantly higher compared to a subsonic flow, although the shear layer is located in the subsonic area of the flow field. Nevertheless, the occurring Mach waves in supersonic jets can give the shear layer sound a high directivity [73]. The self-sustaining feedback loop of supersonic jets is investigated by a multitude of experiments and advanced analyses such as stability theory. Nevertheless, the non-linear interactions and the sound pressure amplitude of screeching are still not fully understood. However, a phenomenological understanding of the aeroacoustic field is sufficient for our purpose to use supersonic jet flow as actuators for IE-measurements.

2.3 Impingement of Supersonic Jets

The flow field and the emitted aeroacoustics of a free jet entering an infinite space of calm air have been discussed. In IE measurements, however, this jet flow is directed to and interacts with a solid surface. This increases the overall sound pressure level by up to 8 dB compared to the free jet flow [81]. This interaction, including the high sound pressure, can lead to surface erosion and unintended vibration of the nozzle or nozzle-connected parts. Not surprisingly, there is a lot of research effort going on in the field of aviation, missile launches, supersonic aircrafts, spaceships, vertical take-off planes, etc. In our application of NDT in civil engineering, we consider the surface plate to be infinite in the lateral direction, so discussion of plate size effects is irrelevant [82].

When a supersonic jet flow is directed towards a flat plate, the axial flow velocity on the plate's surface must become zero. Therefore, the flow in front of the surface is decelerated to subsonic flow velocity by a final normal shock and a recirculation area is formed [82]. This stand-off shock disc is surrounded by the jet flow, which is redirected to the side, including its momentum. Analogous to the screeching sound, the impingement sound is probably also generated by an unsteady shock motion [77]. The generated impingement sound is very intense and can also exceed the local broadband noise by more than 10 dB [82]. Furthermore, in most

cases the impinging jet flow generates a higher sound pressure than the free jet, probably because the recirculation zone introduces additional stronger shock wave fluctuations [76]. The stand-off shock, the recirculation zone, the shock train of the supersonic jet and the Kelvin-Helmholtz instability in the shear layer all contribute to the self-sustaining instability [76, 77, 82, 83]. They all represent sources of sound. However, the underlaying sound production mechanism, including the prediction of discrete frequency tones, are not fully understood due to the high complexity of the aeroacoustic field [77, 82]. Different symmetrical, helical or asymmetrical modes can coexist or cancel each other out [76, 82], leading to staging frequencies of the impingement sound [77]. However, for our adaption to the IE method, only a phenomenological understanding of the impingement sound is required.

The two main parameters governing the impingement noise are the NPR and the distance to the solid surface, the latter being the more significant [77, 82]. No impingement sound was observed at distances smaller than five times the nozzle diameters [76, 77]. It was concluded that the main area for impingement sound generation is between the rear edge of the third and fifth shock cell [76, 84]. For plate distances of more than five nozzle diameters, the impingement reappears with a small frequency shift, which is probably due to a slight variation in the shock train spacing [76]. The larger the plate distance, the less the shock train is affected [76]. The effects of surface roughness were also investigated. The in-air sound pressure generated at a 36 grit sandpaper surface is reduced by 5 dB to 8 dB compared to a smooth surface [85]. The asymmetric modes were observed to be independent of the surface roughness, while the symmetric modes showed variations. This could influence the amplitude of the emitted sound spectrum and the distinct peaks [85]. Nevertheless, a reduction of the in-air sound pressure may mean that more sound energy enters the specimen, which would be advantageous for our NDT purposes. Several studies have also considered impingement sound on inclined plates to angles up to 45° [86]. The aeroacoustic sound remains very similar, so that an application to curved concrete surfaces seems unproblematic. In conclusion, impingement sound frequencies are close to the screeching and the sound amplitude is even higher. The resulting broadband aeroacoustic sound of a supersonic jet flow with high sound pressure is used for continuous contact-free IE actuation.

2.4 Cone of Silence in the Jet's Far Field

While the directivity of screeching and impingement tones is directed upstream due to interference effects of the former [73] and the existing boundary of the latter, the directivity of shear layer sound depends on the influence of the jet flow field on the sound field [87]. Given the radially changing axial flow velocity of a free jet, the local sound propagation velocity varies across the jet due to the superposition of the propagation velocity in quiescent air with the local jet velocity. The radial velocity gradient with maximum on the jet axis causes the acoustic waves to be refracted away from the jet axis. This outward refraction affects all sound sources inside the jet and therefore causes a hollow cone-shaped directivity of the sound generated inside the jet, i.e., the shear layer sound [88]. This effect is sometimes called *cone of silence*. Refraction increases as the distance from the nozzle is increased and can therefore have a large influence on actuators relying on free jet sound that are placed at a large distance to a surface. However, the same effect can also be used to focus the jet sound on the jet axis when using a working fluid that has lower sound propagation velocity than the atmosphere [89]. In these cases, the mixing of the working fluid and the ambient fluid in the turbulent shear layer can create an inward propagation velocity gradient. In air-coupled IE, as well as in most applications, these refraction effects are most important in the downstream direction. In impinging jet setups, it therefore mainly affects the sound generated close to the nozzle, while the sound generated by fluid-wall interaction is not refracted. Depending on the most important sound source for the application, free jet sound or impingement sound, the cone of silence can be a feature that needs to be considered in transducer design.

3 Experimental Setup

3.1 Actuation

The actuator is an ordinary male threaded air nozzle made of steel for compressed air guns (KN-R02-250, SMC Deutschland GmbH, Germany). The standardised nozzles were purchased at a local tool shop, as they are very common in machine shops. The nozzle has a cylindrical connector inside that is 22.4 mm long with a diameter of 8.78 mm. This is followed by a conical part that reduces linearly the diameter to the exiting diameter over a distance of 5.44 mm. This is the convergent part of the nozzle. Different exiting diameters of 1.5 mm, 2 mm and 2.5 mm were tested. Downstream of the convergent part is a straight cylindrical part of 2 mm length leading to the nozzle exit.

Supersonic nozzles generally have a convergent and a divergent part, reaching the critical Mach number of one at the smallest cross-section. The most popular convergent-divergent geometry is the Laval nozzle, as it is supposed to minimise pressure losses. Our air gun nozzles we used have only one convergent part, thus they are not designed as supersonic nozzles. However, due to the flow expansion downstream of nozzle outlet, the potential core of the flow expands. This leads to a self-generated flow divergence that

enables the formation of a supersonic jet flow, which is generated by a convergent nozzle.

The nozzle was connected to the laboratory's pressurised air system with a supply pressure of around 8.5 bar. Between the nozzle and the supply system, a pressure regulator was installed. The desired pressure was set manually using the analogue pressure needle of the manometer.

The reference system from Olsen Instruments is based on a classical impactor that requires physical contact with the surface. In this case, it is a metal cylinder around 3.6 mm long and 5 mm in diameter with a total weight of 6.8 gs. This impactor is designed for use on concrete structure thicknesses of around 75 mm to 450 mm. The company evaluated a contact time for this impactor of around 100 μs to 140 μs.

3.2 Signal Sensing

For the air-coupled measurements, two systems were applied. First, a calibrated microphone was used for the recordings of the baseline measurements. The frequency response of the preamplified 1/4" microphone (MK301 and MV302 by Microtech Gefell GmbH, Germany) with a sensitivity of 5 mV/Pa is nearly linear between 10 Hz and 70 kHz and is calibrated up to 100 kHz. A multifunction I/O device (USB-6361 by National Instruments, USA) was used for data acquisition, recording 200,000 samples at each point with a sample rate of 1 MS/s.

For the measurements on the concrete specimens with air-coupled actuation, an uniaxial accelerometer (352M66 by PCB Piezotronics, USA) was operated with a signal conditioner (480B21 by PCB Piezotronics, USA) with a gain factor of 100, a frequency range of up to 60 kHz and a sensitivity of 11.5 mV/g. Physical contact of the accelerometer with the concrete surface was made with a 1 mm thick double-sided adhesive tape. An 8-bit NI USB-5132 digital storage oscilloscope (National Instruments, USA) combined with Echolyst software (Schweizerischer Verein für technische Inspektionen (SVTI), Switzerland) was used for data acquisition. Each data point consists of 8192 samples recorded at a sample rate of 1 MS/s. Both, the microphone and the accelerometer have been used in previous studies of air-coupled ultrasound actuation [90, 91].

For comparison, a commercially available system, the Olson CTG-2 concrete thickness gauge (Olsen Instruments, USA), was used which excites the concrete structure with a metal cylinder about 5 mm in diameter and senses the resulting waves with an integrated accelerometer. For consistency of the experiments on concrete specimens, the same oscilloscope and acquisition software and settings were used as for the air-coupled measurements. The corresponding IE data acquired with the Olsen system are available online on data repositories for both test specimens [92, 93].

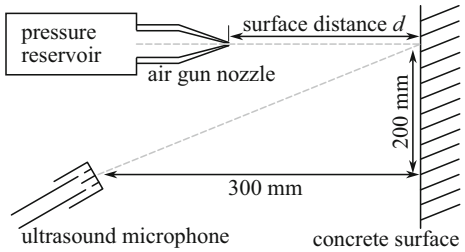

Fig. 3 Schematic of baseline measurements to characterise the acoustics of a jet flow impinging on a concrete surface

3.3 Aeroacoustic Baseline Measurements

For the determination of the optimal nozzle diameter, several baseline measurements were carried out with varying supply pressure and surface distance. The corresponding setup is shown in Fig. 3 as an unscaled schematic. The ultrasound microphone is oriented to the intersection between the concrete surface centre point and the jet axis. The axial distance to the surface is 300 mm and the radial distance is 200 mm, leading to an angle of around 33.7°. The large distance was chosen to reduce the influence of turbulent pressure fluctuations from the shear layer. The distance d between air gun nozzle and the concrete surface was varied in the axial direction between 1 mm and 40 mm, with the microphone remained in a fixed position. The test sample used was a standard concrete cube with an edge length of 250 mm; without any intended cracks or delaminations. For comparison, the free jet without any impingement was also investigated. In this setup, the microphone was oriented perpendicular to the jet axis at a radial distance of 200 mm. As the aeroacoustic field of impingement and screeching shows a high directivity, the spectra of both setups are only qualitatively comparable.

3.4 Test Slabs for Experimental Validation

For experimental validation, two test specimens were used. The first is shown in Fig. 4 before concreting. The foundation is a concrete plate of 1.48 m times 1.48 m and a thickness of 0.3 m. This plate was cast approximately two years before the current measurements started. The surrounding formwork had a height of 100 mm. For a better bonding, the entire surface of the foundation plate was roughened with a pneumatic, multi-bar nailgun. The cover material was cement-based screed, which was purchased as sack bagged goods from a local hardware store. After concreting the screed cover, the test slab was stored in the test hall for more than half a year before the actual measurements started.

Four artificial delaminations were designed with varying concrete cover of 40 mm, 60 mm, 80 mm, and 100 mm. The latter had a cross-section of 0.6 m times 0.6 m and was made of a polyethylene foil fixed with yellow duct tape. The other three

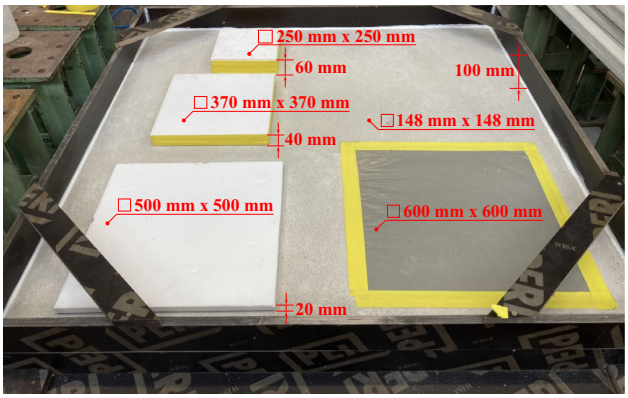

Fig. 4 Photograph of the test specimen called "IE-plate" before concreting

delaminations were initiated by Styrofoam plates of 20 mm, 40 mm, and 60 mm thickness. The higher the concrete cover, the larger the cross-section allowing free IE wave excitation. The size of the cross-section was chosen so that the lateral distance of the centre point is at least three times the concrete cover to all boundaries. The distance between all plates is at least 60 mm and to the formwork at least 80 mm. A detailed drawing can be found online [92]. The measurements were conducted using a grid of 29x29 points with a spacing of 50 mm.

The other test specimen is the so-called "Radar-Platte" and has already been investigated with several methods, including the recently developed Muon tomography. Measurements, drawings, and detailed descriptions can be found in [94]. The measurements were made using a grid of 23x23 points, again with a spacing of 50 mm.

3.5 Data Processing

Once the time signal is recorded, a common FFT transformation to the frequency domain is carried out. To avoid the influence of flexural modes, the resulting spectra were bandpass filtered in the range of 15 kHz to 50 kHz. Then, the peak with the highest amplitude within the bandpass filtered range was picked. The processing was identical for the Olsen system and the air-coupled system.

4 Results

4.1 Spectra and Spectrogram of the Actuation Signal

Baseline measurements were performed to characterise the aeroacoustic field of the supersonic jet flow actuation. The supply pressure was varied by 1 bar, 2 bar, and 4 bar. Distances to the concrete surface of $0 \leq d \leq 40$ mm were investigated. The corresponding spectrograms are shown in Fig. 5a, b, c. For comparison, a free supersonic jet at 2 bar for different downstream positions $0 \leq x* \leq 40$ mm is shown in Fig. 5d. The amplitudes are normalised to the maximum peak value observed in each spectrogram. The maximum value in dB is therefore always zero. Due to this normalisation, only a qualitative comparison between the spectrograms is possible.

At 1 bar in Fig. 5a, the impingement sound occurs at around 39 kHz to 47 kHz at distances of $5 \leq d \leq 17$ mm. The frequency staging is clearly visible and indicates that different modes or wavenumbers dominate the sound generation at varying distances. At higher distances of $d > 17$ mm, no distinct frequencies are observable anymore. Only a very broadband signal between 10 kHz to 70 kHz with decreasing sound pressure amplitude can be recognised.

At 2 bar supply pressure in Fig. 5b, a staging appears again at distances of around $5 \leq d \leq 15$ mm. At higher distances, the maximum sound remains constant at a frequency of 61 kHz, which corresponds to the screeching frequency of a free jet. This indicates that screeching is the sound source and no longer impingement. Although a surface is close by, the distance is high enough to no longer significantly influence the shock train. Furthermore, this screeching peak dominates all adjacent broadband sound by 10 dB or more, and there is no noticeable amplitude decrease between $15 \leq d \leq 40$ mm. This aeroacoustic characteristic appears to be well suited for IE actuation.

In practice, the impingement and screeching sound represent the upper limit for the use of supersonic jets as IE actuator. Once these frequencies appear, they dominate the spectrum independent of the investigated structure. Hence, delaminations emitting S_1-ZGV waves close to these dominant frequencies would remain undiscovered as they are always daubed by the aeroacoustic actuation. Therefore, distances generating impingement sound, including staging, cannot be used. Furthermore, an operation point without screeching would be optimal. In this case, the broadband high-frequency shock sound can also be used to increase the bandwidth of the actuator. If screeching sound is generated, it also acts as an upper limit. In this case, the frequency is very stable. Hence, IE measurements are possible as long as the screeching frequencies are significantly above the highest expected S_1-ZGV wave frequency. At a supply pressure of 1 bar, no screeching is generated. At 2 bar pressure, the screeching occurs at a frequency of 61 kHz. With a safety margin to this natural upper limit of for example 10 %, the maximum frequency for a pressure of 2 bar would be 55 kHz. Roughly estimated, this would lead to a minimum detectable depth of around 36 mm [32]. Thus, shallow delaminations could also be detectable.

At 4 bar supply pressure in Fig. 5c, at distances of $0 \leq d \leq 3$ mm, no distinct impingement frequency is visible. Between $3 \leq d \leq 6$ mm, impingement frequency bands clearly appear. Between $6 \leq d \leq 15$ mm, the impinge-

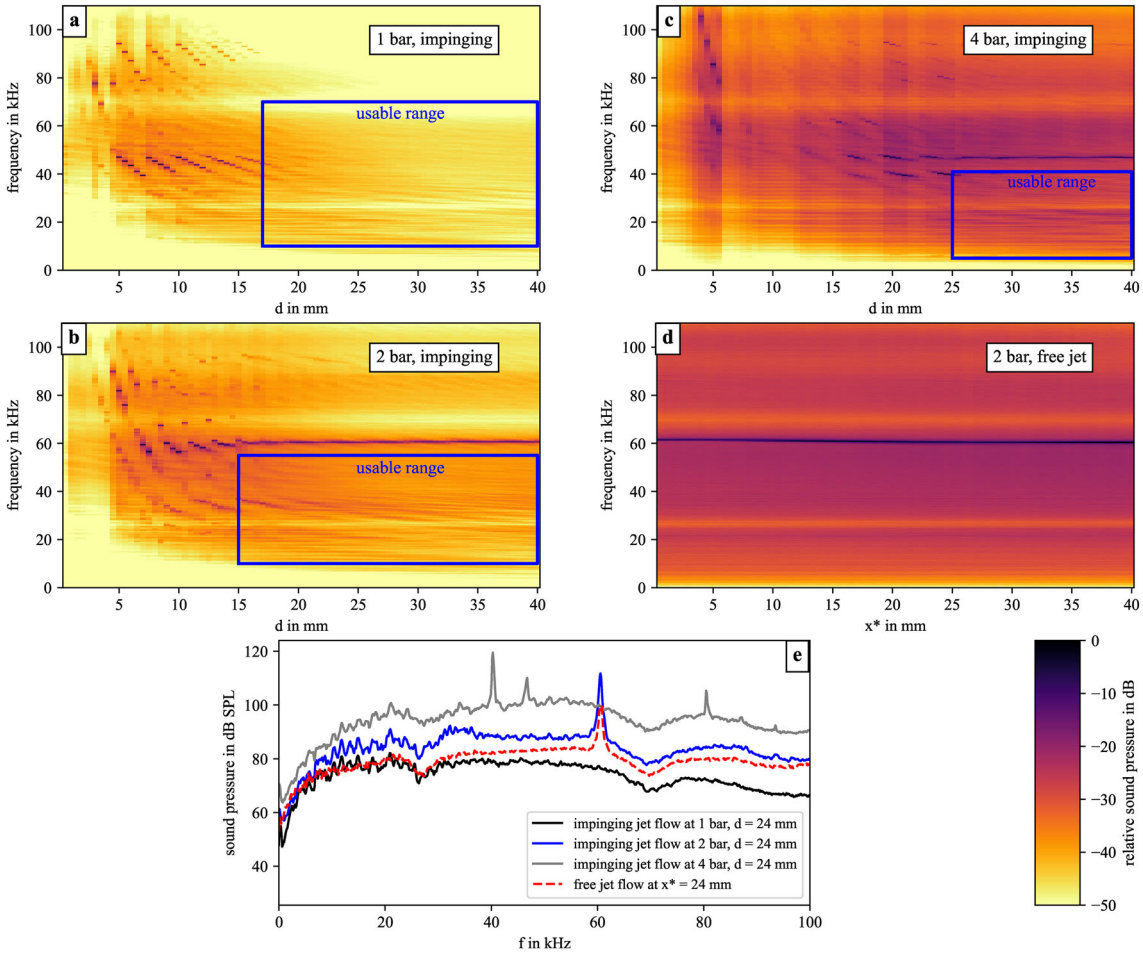

Fig. 5 Aeroacoustic baseline measurements of supersonic jet flow. a: impinging jet at 1 bar; b: impinging jet at 2 bar; c: impinging jet at 4 bar; d: screeching jet at 2 bar; e: comparison of impinging and screeching jet flow at surface distance or downstream position $d = x^* = 24$ mm respectively

ment frequencies become much weaker with sound pressure amplitudes only slightly above the broadband sound. Based on the current data, it remains unclear if impingement is really mitigated or if it is just an effect of the high acoustic directivity of theimpingement sound. At wall distances $15 \leq d \leq 25$ mm, impingement again becomes much more dominant with a kind of binary staging at 39 kHz or 46 kHz. For distances higher than $d > 25$ mm, the transition from impingement to screeching sound is complete and the dominant frequency becomes constant at 46 kHz. Assuming again a safety margin of 10 %, this frequency would lead to a minimum detectable depth of around 48 mm [32], which would already be above the shallowest delamination of 40 mm in the concrete specimen.

In conclusion, the higher the supply pressure, the higher the sound pressure amplitude. In this point, a pressure of 4 bar would be preferable. On the other hand, the impingement frequency decreases with increasing pressure, which hampers the detection of shallow delaminations. At a pressure of 1 bar, there is no impingement sound at distances above 17 mm, which would be preferential. However, a pressure of 2 bar seems to be a good compromise between sound pressure amplitude and impingement frequency, high enough to theoretically detect the shallow delamination.

For comparison, Fig. 5d also shows the free jet flow at 2 bar without an impinging surface. Only at a constant frequency of around 61 kHz a screeching appears. Furthermore, the sound amplitudes also remain almost constant within the measured downstream position of $0 \leq x^* \leq 40$ mm. Based on this comparison, the impinging surface does not influence the shock wave pattern at distances larger 17 mm at 2 bar, which corresponds to a downstream position of around 7 nozzle diameters.

At an axial jet position of 24 mm, the screeching sound is shown in Fig. 5e for all three supply pressures. As expected, the higher the supply pressure, the higher the sound pressure at all frequencies. Furthermore, the impingement sound at 2 bar is added for comparison. As the microphone position

was not identical for both measurements, only a qualitative comparison is possible. The characteristic of both lines is very similar and the frequency range of the peak and the broadband shock sound is identical. In the case of impingement, the shear layer sound seems to drop slightly in comparison to the peak.
To use air-coupled IE actuation for our purpose, 2 bar seems to fulfil the compromise between the sound pressure amplitude and the ability to detect shallow delaminations.

4.2 Spectrum of Received IE Wave Signals

In a first step, the traditional IE actuation with physical contact is compared with a continuous air-coupled jet flow actuation in the centre of the 500 mm times 500 mm delamination with a concrete cover of 80 mm. In both cases, a time window of 1500 μs is considered. Due to the pre-triggering of the Olsen instrument, the real impact occurs after 1600 μs. The S_1-ZGV mode with its corresponding surface oscillation is measured with an accelerometer and shown in Fig. 6a. At 1600 μs a strong peak with a width of around 100 μs is visible. This is partly the contact time of the metal cylinder on the surface, followed by strong Rayleigh waves. At around 1650 μs, a clear oscillation starts more than 28 periods. With increasing time, the amplitude decreases. The entire signal evolution is very typical and representative for IE measurements actuated by physical contact. Based on a common FFT analysis, the corresponding spectrum of the signal is derived. A clear peak is visible at 20 kHz. This measurement is also used to calibrate the wave velocity. With a known concrete cover of 80 mm and a correction factor of $\beta = 0.95$, this frequency yields a pressure wave velocity of $c_p = 3400$ ms. However, not only the S_1-ZGV wave is actuated. Several peaks below 5 kHz are visible as well (no bandpass filter was used for these two spectra). These low-frequency oscillations are probably generated by flexural modes. Due to the inertia and contact time of the metal cylinder, modes in the low-frequency range can be actuated as well. Furthermore, a small plateau of increased amplitude appears between 25 kHz and 32 kHz. Above 32 kHz only random noise is measured.

In Fig. 6b, the air-coupled jet flow actuation is shown at the same spatial position and was recorded with the same sensing devices. First of all, it is clearly seen that this signal has no distinct beginning or ending, as the supersonic jet flow is generated continuously. Furthermore, the signal has a lower amplitude (less than a tenth) and appears to be more noisy. The higher noise-level is probably caused by interfering Rayleigh waves, as these wave modes are generated continuously as well. So far, a clear sinusoidal signal cannot be identified. However, the corresponding spectrum shows a clear peak at the S_1-ZGV mode frequency of 20 kHz. As the entire time signal has a lower amplitude, the amplitude of the peak in the spectrum is also smaller compared to physical contact. Advantageously, the air-coupled actuation peak has a much higher distance to any secondary peak. For physical contact, the S_1-ZGV mode and several flexural modes have almost the same peak amplitude.
The improved first to secondary peak ratio in the case of jet flow actuation results directly from the actuation method. The spectrogram in Fig. 5 for 2 bar at a surface distance of 24 mm shows an increased sound pressure between 10 kHz and 100 kHz. On the other hand, below 5 kHz, the amplitude decreases rapidly. If the actuation does not contain such low-frequency components, low-frequency modes within the sample cannot be amplified. Consequently, no flexural modes appear, which is confirmed by the spectrum in Fig. 6b. On the other hand, high-frequency fragments do appear, e.g., between 37 kHz and 40 kHz. It is unclear if this is caused by the flow field or by high-harmonic oscillations of the solid structure. However, the physical contact is not even able to excite such higher harmonics (see 6a).
The use of supersonic jet flow provides continuous air-coupled IE actuation. The frequency peak appears exactly at the same position where it would be excited in the case of physical contact. This shows that jet flow is well suitable to excite the S_1-ZGV wave while no low-frequency flexural modes are excited.

4.3 Actuator Distance and Input Pressure

Based on the previous point measurement, it was shown that the supersonic jet flow continuously excites the IE mode with a clear frequency peak. Now the question remains, which supply pressure and which surface distance give the best results. Thus, both parameters were varied in the centre of the 500 mm times 500 mm delamination with 80 mm concrete cover to find the best setting.
First, a supply pressure of 1 bar, 2 bar, and 4 bar was applied and evaluated as shown in Fig. 7. The air-coupled measurements were repeated 100 times, recording 8192 samples at a sampling rate of 1 MS/s. All 100 time frames were analysed and the respective peak frequencies were picked to calculate the corresponding percentiles. In Fig. 7a, the red bar represents the median value, the lower and upper edges of the black boxes are the first and third quartile, and the black bars at the lower and upper ends of the line depict the 5 % and 95 % percentile.
At 1 bar and 1 mm distance, a clear deviation from the expected frequency is observed. The expected frequency is already measured at 2 mm to 4 mm,. At this short distance, the shock wave pattern is not yet fully developed, but already able to excite the S_1-ZGV mode. Nevertheless, the actuation seems to be rather unstable, as the standard deviation is quite large. Much higher frequencies are observed between 5 mm and 13 mm. These are exactly the staging frequencies of the impingement sound, as already shown in Fig. 5a.

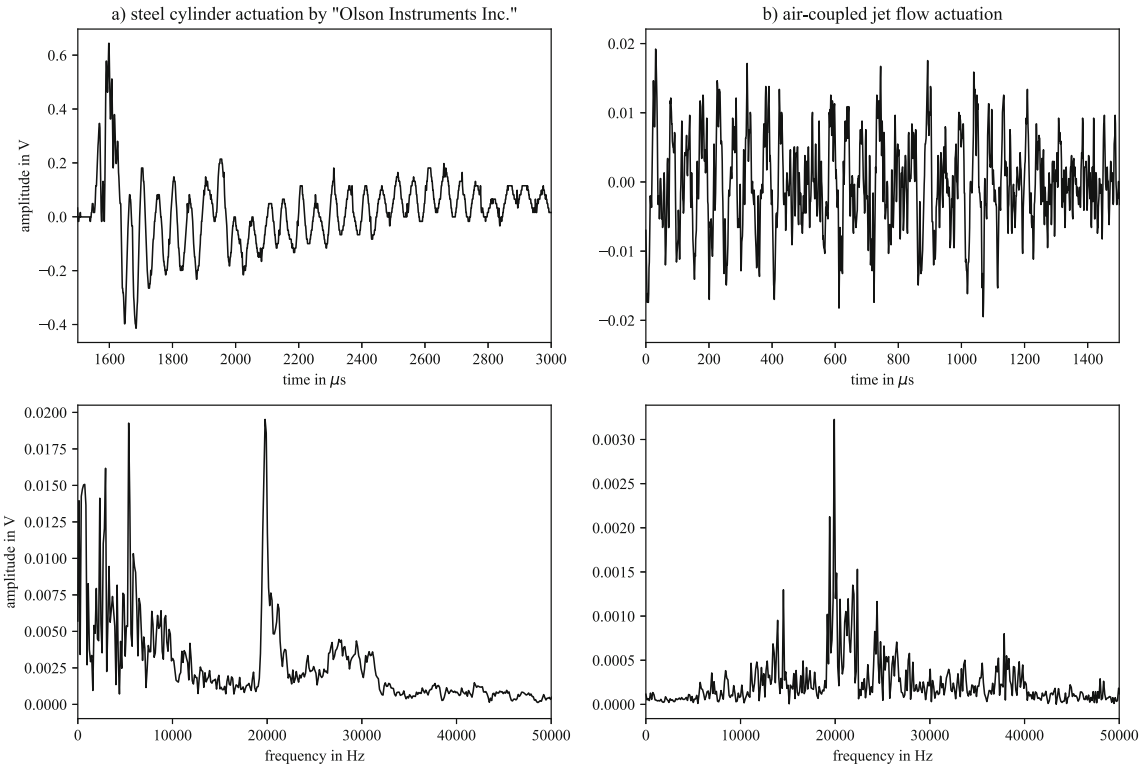

Fig. 6 Time signal and corresponding spectrum above the centre of the 80 mm delamination. **a** metal cylinder actuation by "Olson Instruments Inc."; **b** continuous air-coupled jet flow actuation

These frequencies dominate the acoustic field, and the corresponding Rayleigh waves on the surface probably daub the S_1-ZGV mode. The tiny (not visible) standard deviation between 5 mm and 11 mm confirms the high domination of the staging sound. At 12 mm and 13 mm, the lower 5 % percentile is exactly on the level of the expected frequencies. This might indicate that at least in some measured time periods, the S_1-ZGV mode was able to persist. At distances of 14 mm to 40 mm, the air-coupled actuation generates the S_1-ZGV mode, as shown in Fig. 7a.

At 2 bar, a similar trend is visible in Fig. 7b. Again, at distances between 1 mm to 4 mm, the S_1-ZGV mode is already excited, although the shock wave train does not have enough space to fully develop. Between 7 mm to 12 mm, the staging of impingement sound in agreement to Fig. 5b dominates again. At a distance greater than 13 mm in Fig. 7b, the S_1-ZGV mode is excited again, except at 17 mm. Nevertheless, the standard deviation between 5 mm to 20 mm is fairly high, indicating unstable actuation or time-varying mode conversion. At distances greater than 21 mm, the median is close to the expected frequency and the standard deviation remains small.

Fig. 7c shows the actuation with 4 bar supply pressure. Between 1 mm to 11 mm, the measured dominant frequency is significantly below the S_1-ZGV mode frequency. The reason for this remains unclear as the staging frequencies of the impingement sound are generated at much higher frequencies. Between 12 mm to 28 mm, the impingement frequencies become dominant and the standard deviation increases drastically. At distances greater than 28 mm, the S_1-ZGV wave is excited and the standard deviation is very small, indicating a stable actuation.

Based on the measurements shown, all three pressure levels are able to excite the S_1-ZGV mode. The corresponding sound pressure amplitudes in the frequency range of interest is approximately between 70 dB SPL at 1 bar and 100 dB SPL at 4 bar supply pressure (as shown in Fig. 5e). These pressure levels are significantly lower compared to electric spark sources for non-contact impulse actuation with around 178 dB SPL [55]. However, a continuous actuation based an impinging jet flow with 70 dB SPL seem to be already sufficient to generate qualitatively similar results. At 1 bar and 2 bar the S_1-ZGV mode is already excited at distances of around 14 mm, whereas at 4 bar the minimum distance is already 28 mm. On the other hand, the sound pressure level is significantly higher at 2 bar compared to 1 bar. Therefore, we consider a 2 bar actuation as the best compromise between sound pressure and proximity to the surface. Hence, all measurements are carried out with a 2 bar supply pressure in the following.

With a fixed supply pressure of 2 bar, the other parameter is the distance to the surface. To investigate its influence,

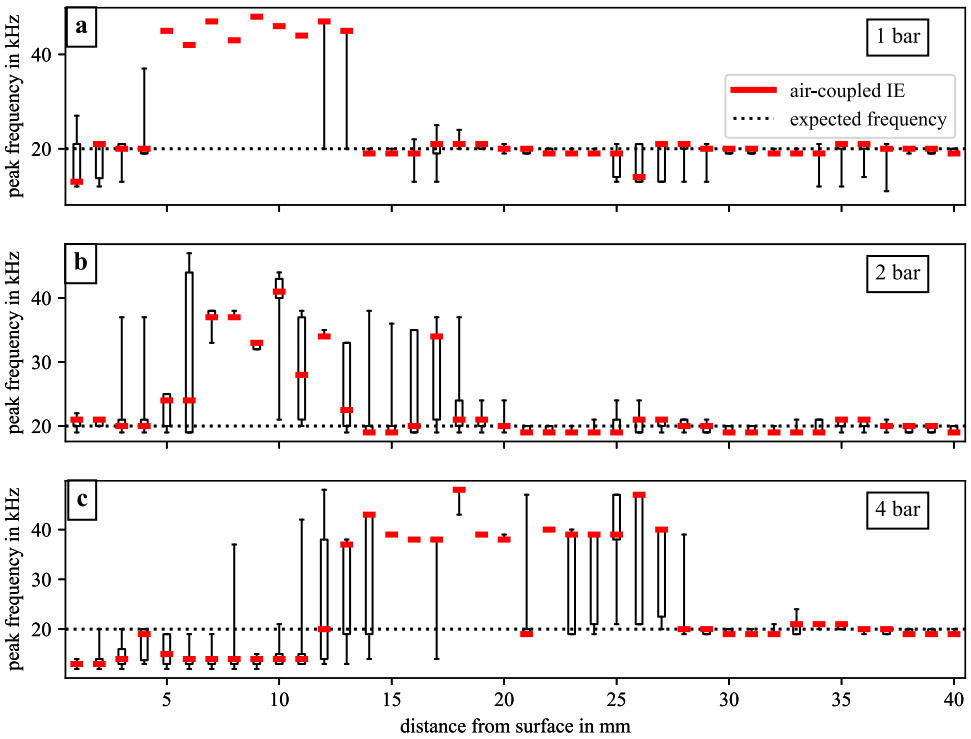

Fig. 7 Continuous air-coupled IE actuation with a supersonic jet flow in the centre of a 500 mm times 500 mm delamination with 80 mm concrete cover for supply pressures of 1 bar, 2 bar, and 4 bar and varying distances

the nozzle was always positioned in the centre of the four delaminations with a concrete cover of $t = 40$ mm, 60 mm, 80 mm, and 100 mm. Then, the distance was varied again between 1 mm and 40 mm.

Fig. 8 shows the measurement results. Again, the red bar symbolises the median value of the 100 measurements, framed by a box plot visualising the standard deviation. With decreasing concrete cover, the expected frequency of the S_1-ZGV wave increases. The requirement for an acceptable measurement distance is that the S_1-ZGV mode is excited and the standard deviation is small. For a concrete cover of 100 mm, distances above 23 mm are promising (8a) and for $t = 80$ mm, distances above 21 mm are sufficient (8b). In the case of $t = 60$ mm, the S_1-ZGV mode already appears above a distance of 18 mm for most points, however, the standard deviation remains high (8c). Only at 24 mm and 28 mm is the standard deviation small. The closer the nozzle, the higher the sound pressure. For these three thicknesses of concrete cover, the best compromise seems to be at the distance of 24 mm. Figure 8d shows the results for $t = 40$ mm. Below 4 mm and above 18 mm, the dominant frequency is not the S_1-ZGV mode. This frequency of around 13 kHz is even lower than for a concrete cover of 100 mm with 16 kHz. The source for this frequency remains unclear. Between 5 mm to 17 mm, the expected frequency is met or quite close to it. Nevertheless, these measured dominant frequencies are also very close to the staging of the impingement sound shown in Fig. 5c. The characteristic staging trend is visible three times, starting at 7 mm, 10 mm and 16 mm, respectively. It seems as if this match with the expected frequency happens coincidentally. In fact, the used nozzle is not able to excite the S_1-ZGV mode for a shallow delamination of 40 mm depth. Thus, we remain at a distance to the surface of 24 mm for all further measurements.

4.4 Comparison of Air-Coupled and Physical Contact Actuation

A supply pressure of 2 bar at a distance of 24 mm seems to be the best compromise. With this setting, the two concrete specimens are measured. The Olsen IE device serves as reference.

The colour plot in Fig. 9a represents the dominant frequency measured with Olsen IE device of the concrete specimen shown in Fig. 4. The four blue rectangles indicate the four intruded delaminations. The test specimen foundation is 300 mm with a cover layer of 100 mm on top, including the artificial delaminations. In Fig. 9a, it is clear to see that the frequency of the delamination with $t = 100$ mm is equal to the "non-delaminated" part of the specimen. In fact, there is no point on the entire specimen where we could measure the full thickness of 400 mm. Although the surface of the specimen foundation was roughened with a pneumatic multi-bar nail gun, the bonding to the top layer seems to be weak and/or the acoustic properties of both layers deviate too much so that most of the signal energy is reflected. Therefore, 100 mm is considered as the maximum depth. At $t = 60$ mm and $t = 80$ mm delamination, the change in frequency is sig-

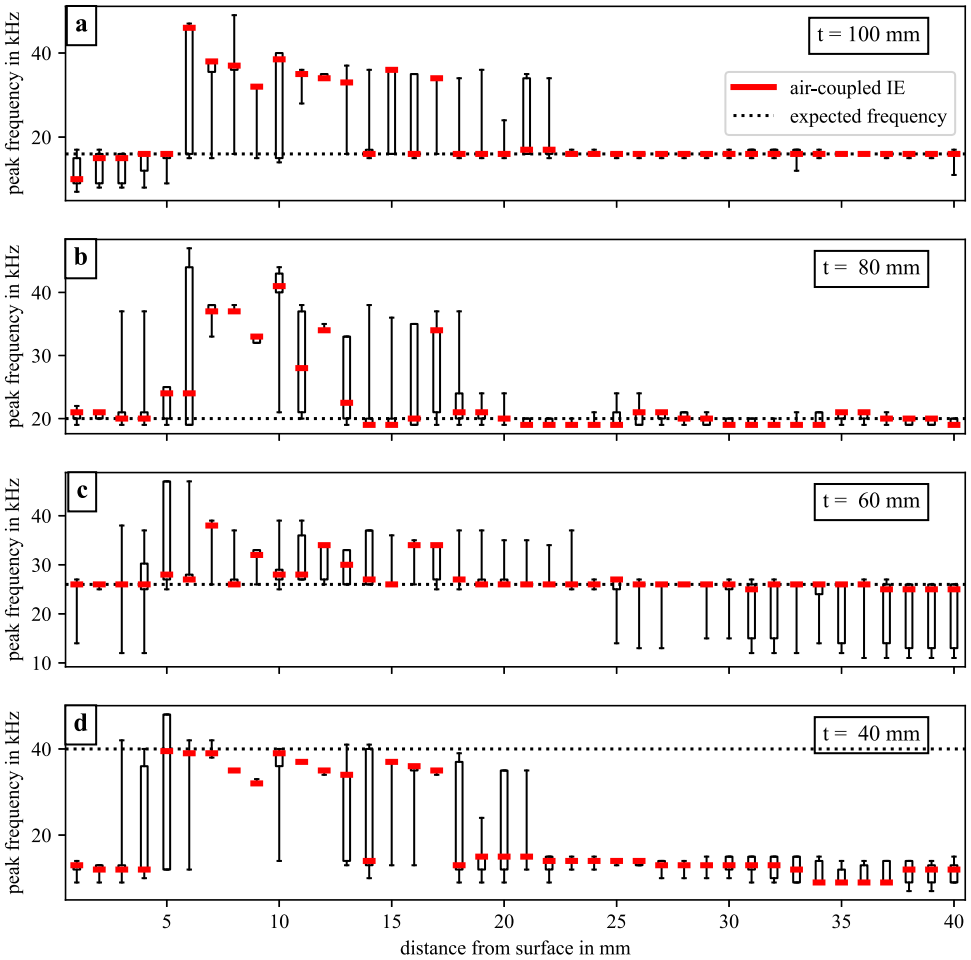

Fig. 8 Continuous air-coupled IE actuation with a supersonic jet flow in the centre of the four delaminations with 40 mm, 60 mm, 80 mm and 100 mm concrete cover at varying distances and 2 bar supply pressure

nificant. Both can be identified in position and size by eye. The shallow delamination of $t = 40$ mm is not detectable. The impactor was designed for concrete thicknesses above 75 mm, so the detection of the 60 mm delamination is already close to the lower limit. These IE measurements performed with the Olsen IE device are considered as our reference for the air-coupled actuation. The entire data set is available in an online repository [92].

For comparison, three lines with identical spacing of sampling points were measured with air-coupled actuation and marked as green lines in Fig. 9a. The first line is parallel to the x-axis at y= 350 mm and the results are presented in Fig. 9b. Along this line, three delaminations are crossed. Above the shallow delamination of $t = 40$ mm at 120 mm$\leq x \leq$ 370 mm, the expected frequency is the highest. Here, even the air-coupled actuation is not able to excite the expected frequency of 40 kHz. On the other hand, the air-coupled and the Olsen IE frequencies are close to each other and fluctuate around 16 kHz, which would correspond to a concrete cover of $t = 100$ mm. At 430 mm$\leq \times \leq$ 800 mm, the next delamination of $t = 60$ mm is crossed. Here the air-coupled and the Olsen IE show a high correlation and the values are close to the expected frequency of 27 kHz. A similar behaviour is seen for $t = 80$ mm at 860 mm$\leq \times \leq$ 1360 mm. Interestingly, the small jetty between both delaminations at 800 mm$\leq \times \leq$ 860 mm is recognised by both actuation methods as well. The width of this jetty of 60 mm is smaller than its height of 100 mm. For such a geometric ratio, one would not expect the formation of a S_1-ZGV mode. Even at 1450 mm, the 16 kHz corresponding to $t = 100$ mm is detected, although this measurement point is only 30 mm away from the outer edge of the specimen. Based on this comparison, the air-coupled IE generates the same frequencies and depth information as the physical contact IE.

The two other lines were measured parallel to the y-axis at x= 600 mm and x= 1150 mm respectively. In Fig. 9c, the $t =$ 60 mm delamination is crossed and in Fig. 9d, the $t = 80$ mm delamination. In both cases, the Olsen IE and the air-coupled IE show a high correlation with each other and are close to the expected frequencies. In Fig. 9c, there are four data points with increased frequency at 750 mm$\leq$y$\leq$ 900 mm. At least at one point, Olsen IE shows the same increased frequency. Interestingly, Fig. 9a shows an area of increased frequencies of around 20 kHz right in this region at around x=y=750 mm.

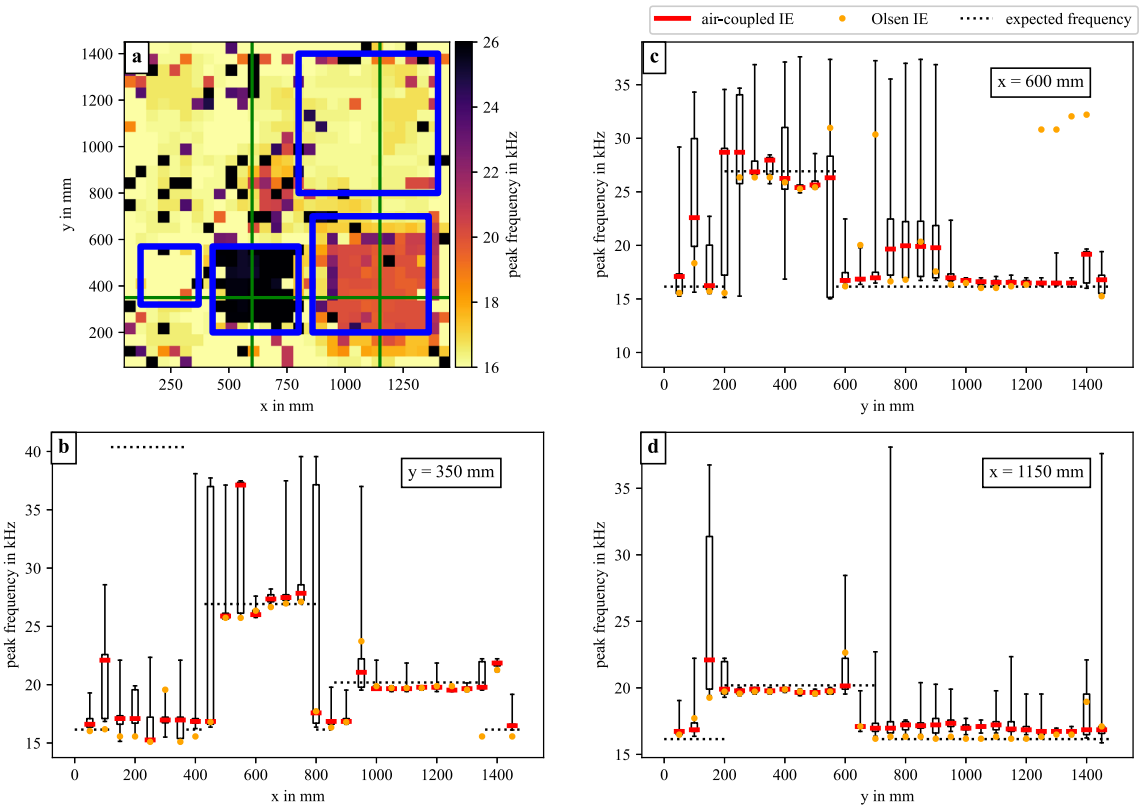

Fig. 9 Experimental results of the concrete specimen "IE plate". **a** frequencies measured by IE with physical contact, blues squares indicate the delaminations; **b** air-coupled IE results at y = 350 mm; **c** air-coupled IE results at x = 600 mm; **d** air-coupled IE results at x = 1150 mm

Thus, the air-coupled device seems to be sensitive to this small area of (unknown) increased frequencies as well. On the other hand, at 1250 mm≤y≤ 1400 mm in Fig. 9c, the IE with physical contact measures frequencies of 30 kHz, whereas the air-coupled IE remains at the expected 16 kHz level. As we do not know the "true" value, we cannot decide at this point which frequency is the correct one. However, both systems show high sensitivity and reliability.

In conclusion, the air-coupled IE results correlate highly to Olsen IE and are close to the expected frequencies except for the shallow delamination of $t = 40$ mm. Furthermore, the air-coupled IE based on supersonic jet flow detects the small jetty between the delaminations and measures the correct concrete cover of $t = 100$ mm with only 30 mm distance to the specimen outer edge. This indicates that the air-coupled IE is a robust and reliable actuation approach.

Measurements with air-coupled IE and Olsen IE on a second test specimen are shown in Fig. 10. The specimen is 200 mm thick and in described in detail in [94]. Besides a delamination, an empty cladding tube is also embedded. The expected frequencies are computed based on a pressure wave velocity of 4250 m/s and β =0.95. No frequency is given around the cladding tube, as this type of geometry is not in the scope of classical IE theory, as the assumption of a plate-like structure in not fulfilled.

Based on a 50 mm grid, Olsen IE measurements [92] were taken as reference and are shown in the colour plot in Fig. 10a. The delamination is clearly detected by the increase in frequency from around 10 kHz to 13.5 kHz. Near to the cladding tube, a frequency decrease to around 8 kHz is observed. The empty cladding tube could be interpreted as a local increase in porosity. Thus, the elastic properties and consequently the pressure wave velocity change in this area. Thus, we probably still excite a S_1-ZGV mode that is affected by the full specimen thickness of 20 mm, but with a reduced local pressure wave velocity. Therefore, the measured frequency decrease is reasonable, although a distinct frequency value cannot be calculated based on IE theory. The shown data can be found online in a data repository [93].

Similar to the first specimen, three lines were measured with air-coupled IE, which are indicated as green lines in Fig. 10a. The first line is parallel to the x-axis at y= 300 mm. This line crosses the delamination in the centre (see Fig. 10b). Along the delamination, both approaches of IE actuation highly correlate and coincide with the expected frequency. On the contrary, in the non-delaminated area, only Olsen IE excited the S_1-ZGV mode. The air-coupled IE shows much

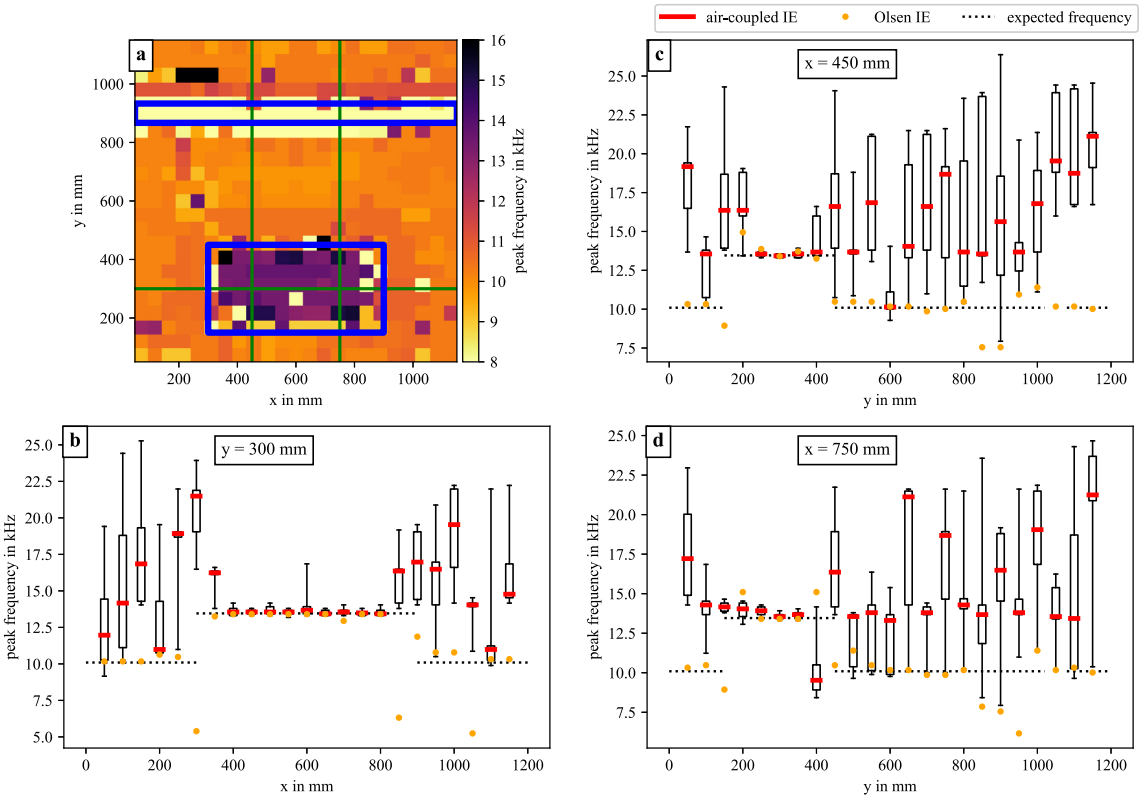

Fig. 10 Experimental results of the concrete specimen "Radar plate". **a** frequencies measured by IE with physical contact, blues squares indicate the delamination and the cladding tube; **b** air-coupled IE results at y = 300 mm; **c** air-coupled IE results at x = 450 mm; **d** air-coupled IE results at x = 750 mm

higher frequencies with high fluctuations of the median value and high standard deviation. As shown in Fig. 5b and e, the sound pressure amplitude at 2 bar and $d = 24$ mm decreases significantly below approximately 10 kHz. Therefore, we believe that the actuator energy in this required frequency range is insufficient to excite the S_1-ZGV mode. Measuring at 4 bar or just with a larger nozzle might overcome this issue. On the other hand, this confirms our statement based on the spectrum in Fig. 6b that air-coupled IE does not excite low-frequency flexural modes, since the entire spectrum is shifted to higher frequencies compared to theclassical IE with mechanical impactors.

The other two lines parallel to the y-axis at x= 450 mm and x= 750 mm show very similar trends. Above delamination, both actuation approaches highly correlate with each other and with the expected frequency. In the non-delaminated areas, the air-coupled IE does not deliver enough actuation energy to excite the S_1-ZGV mode of the 200 mm thick specimen. As the frequency around the cladding tube further decrease to around 8 kHz at y= 900 mm, the air-coupled actuation is again not able to excite these low-frequencies.

The air-coupled IE shows a high correlation to the physical contact IE for both concrete specimens. Even small structures as the jetty between the delaminations are recorded. Furthermore, a concrete cover of 100 mm is correctly measured with only 30 mm distance to the outer edge of the specimen. All this proves the high sensitivity and reliability of air-coupled IE actuation based on supersonic jet flow.

5 Conclusion

A completely new approach for continuous air-coupled IE actuation is developed and experimentally validated. A supersonic jet flow generates a high-amplitude broadband noise. In this study, we did not consider the aeroacoustic field as noise. On the contrary, we use the aeroacoustic sound as an actuator for IE measurements. To the best knowledge of the authors, this is the first time that broadband impingement sound generated by a supersonic jet flow has been used for non-destructive testing and evaluation in civil engineering.

A convergent nozzle geometry with a cylindrical outlet of 2.5 mm in diameter was operated at different supply pressures and surface distances. A 2 bar supply pressure and a 24 mm distance to the surface are considered to be the best compromise between sound pressure amplitude and achievable frequency bandwidth.

Two concrete specimens were investigated with this setting. Both specimens contained delaminations with concrete cover thicknesses between 40 mm and 150 mm. The air-coupled results were compared to classical IE measurements with a physical contact. Both IE approaches show high correlation with each other and with the expected frequencies. Although the shallow delamination of 40 mm was not recognised by either system, all other delaminations were found in correct spatial extent and with correct concrete cover thickness by both systems. Even small structures like the jetty between two delaminations were found. This proves the high sensitivity and reliability of air-coupled IE actuation based on supersonic jet flow. The results are very promising and enable a continuous IE actuation, which may drastically increase the measurement speed of IE. Fully automatised or multi-channel systems could be developed. Such systems would be very robust and cheap as no moving parts are required for actuation, only a static nozzle driven by pressurised air. Furthermore, the nozzle operates in any direction. Thus, masonry or ceilings can also be investigated easily and continuously. The results are very promising, although a sub-optimal off-the-shelf nozzle geometry was used, which was not designed to generate supersonic flow. With a real convergent-divergent geometry like a Laval nozzle, the pressure losses could be reduced significantly, which would probably increase the aeroacoustic sound pressure. Large nozzle lips would also be preferable for high sound pressure. To excite lower frequencies to investigate large specimen thicknesses, larger nozzle diameters should be tested. To achieve an even wider frequency bandwidth, one could also explore the working conditions of new nozzle designs that do not produce screeching sound and also allow the use of high-frequency, broadband shock sound. Another possible approach is to design a multi-nozzle system with different supersonic jets next to each other.

Due to continuous actuation, we see huge potential to accelerate IE measurements in the future. Multi-nozzle systems installed on inspection trucks could run at full driving speed. Thus, entire highways can be non-destructively tested and evaluated within hours, leading to a more reliable transport infrastructure.

Acknowledgements We would like to thank Sean Smith and Marco Lange for manufacturing and preparation of the concrete specimens.

Author Contributions Conception and creation of the entire text and all figures as well as proofreading (including references) are free of artificial intelligence based software or large language models. All content is generated by humans.

All authors have contributed substantially to the work reported in this publication. Conceptualization: C.S.; methodology: C.S. and B.B.; software: B.B.; validation: C.S. and B.B.; formal analysis: B.B.; experimental setup: B.B.; data recording: B.G.; data curation: C.S., B.B. and B.G.; resources: C.S.; writing—original draft preparation: C.S.; writing—review and editing: C.S., B.B. and B.G.; visualization: C.S. and B.B.; supervision: C.S. and B.B.; project administration: B.B. All authors have read and agreed to the published version of the manuscript.

Funding Open Access funding enabled and organized by Projekt DEAL.

Availability of Data and Materials The impact-echo data used for validation are available online in a data repository under a Creative Commons Attribution (CC BY) license: Impact-echo data of the "IE Platte" doi: 10.7910/DVN/EH4E9G [92] and impact-echo data of the "Radar Platte" doi: 10.7910/DVN/UNOH2U [93]. Other data or scripts are available on request. Access to the concrete specimens will be granted on request.

Declarations

Conflict of Interest The author declare no conflict of interest or competing interests.

Ethics Approval and Consent to Participate Not applicable.

Consent for Publication All authors have proof-read the final version of this manuscript. All authors have agreed to the published version of the manuscript.

Authors' information Not applicable.

References

1. Capros, P., De Vita, A., Florou, A.: EU reference scenario 2020-energy, transport and GHG emissions trends to 2050. Technical report, European Commission (2020)
2. Bundestag, D.: Stand der Modernisierung von Brücken der Bundesfernstraßen. Technical report, Bundesministerium für Verkehr und Infrastruktur (2020)
3. Milani, L., Mohr, D., Sandri, N.: Built to last: Making sustainability a priority in transport infrastructure. McKinsy & Company **3** (2021)
4. Schulz, W.H., Mainka, M.: Gesamtwirtschaftliche Bewertung der Sperrung der A1-Rheinbrücke für den Lkw-Verkehr. Technical report, Pro Mobilität - Initiative für Verkehrsinfrastruktur (2013)
5. Song, H.-W., Saraswathy, V.: Corrosion monitoring of reinforced concrete structures - A review. Int. J. Electrochem. Sci. **2**, 1–28 (2007)
6. Greve-Dierfeld, S., Lothenbach, B., Vollpracht, A., Wu, B., Huet, B., Andrade, C., Medina, C., Thiel, C., Gruyaert, E., Vanoutrive, H., et al.: Understanding the carbonation of concrete with supplementary cementitious materials: a critical review by RILEM TC 281-CCC. Mater. Struct. **53**(136), 1–34 (2020). https://doi.org/10.1617/s11527-020-01558-w

7. Saouma, V.E. (ed.): Diagnosis and Prognosis of AAR Affected Structures: State-Of-the-Art Report of the RILEM Technical Committee 259-ISR vol. 31. Springer, Germany (2020). https://doi.org/10.1007/978-3-030-44014-5
8. Figueira, R.B., Sousa, R., Coelho, L., Azenha, M., Almeida, J.M., Jorge, P.A.S., Silva, C.J.R.: Alkali-silica reaction in concrete: Mechanisms, mitigation and test methods. Constr. Build. Mater. **222**, 903–931 (2019). https://doi.org/10.1016/j.conbuildmat.2019.07.230
9. Malone, C., Sun, H., Zhu, J.: Nonlinear impact-echo test for quantitative evaluation of ASR damage in concrete. J. Nondestruct. Eval. **42**(4), 93 (2023). https://doi.org/10.1007/s10921-023-01003-2
10. Taylor, H.F.W., Famy, C., Scrivener, K.L.: Delayed ettringite formation. Cem. Concr. Res. **31**(5), 683–693 (2001). https://doi.org/10.1016/S0008-8846(01)00466-5
11. Sansalone, M., Carino, N.J.: Detecting delaminations in concrete slabs with and without overlays using the impact-echo method. Mater. J. **86**(2), 175–184 (1989). https://doi.org/10.14359/2350
12. Azari, H., Lin, S.: Evaluation of the impact echo method for concrete bridge decks with asphalt overlays. Transp. Res. Rec. **2673**(2), 436–444 (2019). https://doi.org/10.1177/0361198119828
13. Ke, Y.-T., Cheng, C.-C., Lin, Y.-C., Ni, Y.-Q., Hsu, K.-T., Wai, T.-T.: Preliminary study on assessing delaminated cracks in cement asphalt mortar layer of high-speed rail track using traditional and normalized impact-echo methods. Sensors **20**(11), 3022 (2020). https://doi.org/10.3390/s20113022
14. Kee, S.-H., Oh, T., Popovics, J.S., Arndt, R.W., Zhu, J.: Nondestructive bridge deck testing with air-coupled impact-echo and infrared thermography. J. Bridge Eng. **17**(6), 928–939 (2012). https://doi.org/10.1061/(ASCE)BE.1943-5592.0000350
15. Maierhofer, C.: Nondestructive evaluation of concrete infrastructure with ground penetrating radar. J. Mater. Civil Eng. **15**(3), 287–297 (2003). https://doi.org/10.1061/(ASCE)0899-1561(2003)15:3(287)
16. Saarenketo, T., Scullion, T.: Road evaluation with ground penetrating radar. J. Appl. Geophys. **43**(2), 119–138 (2000). https://doi.org/10.1016/S0926-9851(99)00052-X
17. Wong, P.T.W., Lai, W.W.L., Sham, J.F.C., Poon, C.-S.: Hybrid nondestructive evaluation methods for characterizing chloride-induced corrosion in concrete. NDT & E Int. **107**, 102123 (2019). https://doi.org/10.1016/j.ndteint.2019.05.008
18. ASTM International: Standard practice for measuring delaminations in concrete bridge decks by sounding. D4580 / D4580M - 12 (2018) https://doi.org/10.1520/D4580_D4580M-12R18
19. Oh, T., Popovics, J.S., Sim, S.-H.: Analysis of vibration for regions above rectangular delamination defects in solids. J. Sound Vib. **332**(7), 1766–1776 (2013). https://doi.org/10.1016/j.jsv.2012.11.003
20. Gucunski, N., Imani, A., Romero, F., Nazarian, S., Yuan, D., Wiggenhauser, H., Shokouhi, P., Taffe, A.: Nondestructive Testing to Identify Concrete Bridge Deck Deterioration. Transp. Res. Board (2013)
21. Zhang, G., Harichandran, R.S., Ramuhalli, P.: Application of noise cancelling and damage detection algorithms in NDE of concrete bridge decks using impact signals. J. Nondestruct. Eval. **30**(4), 259–272 (2011). https://doi.org/10.1007/s10921-011-0114-8
22. Fletcher, P.B., Pellonpaa, C.V., Meyers, H., Vivian, W.E., Woodford, J.P.: Instruction manual for bridge deck delamination detector. technical report, Michigan department of state highways and transportation (1977). Michigan Department of State Highway and Transportation
23. Hendricks, L.J., Baxter, J.S., Chou, Y., Thomas, M., Boekweg, E., Guthrie, W.S., Mazzeo, B.A.: High-speed acoustic impact-echo sounding of concrete bridge decks. J. Nondestruct. Eval. **39**(58), 1–12 (2020). https://doi.org/10.1007/s10921-020-00695-0
24. Sun, H., Pashoutani, S., Zhu, J.: Nondestructive evaluation of concrete bridge decks with automated acoustic scanning system and ground penetrating radar. Sensors **18**(6), 1955 (2018). https://doi.org/10.3390/s18061955
25. Dorafshan, S., Azari, H.: Deep learning models for bridge deck evaluation using impact echo. Constr. Build. Mater. **263**, 120109 (2020). https://doi.org/10.1016/j.conbuildmat.2020.120109
26. Miwa, T.: Non-destructive and quantitative evaluation of rebar corrosion by a vibro-Doppler radar method. Sensors **21**(7), 2546 (2021). https://doi.org/10.3390/s21072546
27. Miwa, T., Nakazawa, Y.: Nondestructive evaluation of localized rebar corrosion in concrete using vibro-radar based on pulse Doppler imaging. Remote Sens. **14**(18), 4645 (2022). https://doi.org/10.3390/rs14184645
28. Grohmann, M., Müller, S., Niederleithinger, E., Sieber, S.: Reverse time migration: Introducing a new imaging technique for ultrasonic measurements in civil engineering. Near Surf. Geophys. **15**(3), 242–258 (2017). https://doi.org/10.3997/1873-0604.2017006
29. Köhn, D., Meier, T., Fehr, M., De Nil, D., Auras, M.: Application of 2D elastic Rayleigh waveform inversion to ultrasonic laboratory and field data. Near Surf. Geophys. **14**(5), 461–467 (2016). https://doi.org/10.3997/1873-0604.2016027
30. Sansalone, M.J., Streett, W.B.: Impact-echo: Nondestructive Evaluation of Concrete and Masonry. Bullbrier Press, Ithaca, New York (1997)
31. Carino, N.J.: The impact-echo method: an overview. In: Structures 2001: Proceedings of the 2001 Structures Congress & Exposition, Washington, D.C., pp. 1–18 (2001). https://doi.org/10.1061/40558(2001)15
32. Forde, M.C.: Report on nondestructive test methods for evaluation of concrete in structures. Technical report ACI 228.2R-13, American Concrete Institute (2013)
33. Carino, N.J., Sansalone, M., Hsu, N.N.: Flaw detection in concrete by frequency spectrum analysis of impact-echo waveforms. Int. Adv. Nondestruct. Test. **12**, 117–146 (1986)
34. Carino, N.J., Sansalone, M., Hsu, N.N.: A point source-point receiver, pulse-echo technique for flaw detection in concrete. ACI J. 83(2), 199–208 (1986). https://doi.org/10.14359/10414
35. Sansalone, M., Carino, N.J.: Impact-echo: A method for flaw detection in concrete using transient stress waves. technical report, NBSIR 86-3452, National Bureau of Standards, Washington, DC (1986)
36. Zhu, J., Popovics, J.S.: Air-coupled impact-echo method for NDT of concrete. In: 32th Annual Review of Progress in Quantitative Nondestructive Evaluation, 2005, Brunswick, Maine, USA, vol. 820, pp. 1351–1357 (2006)
37. Zhu, J., Popovics, J.S.: Imaging concrete structures using air-coupled impact-echo. J. Eng. Mech. **133**(6), 628–640 (2007). https://doi.org/10.1061/(ASCE)0733-9399(2007)133:6(628)
38. Liang, M.-T., Su, P.-J.: Detection of the corrosion damage of rebar in concrete using impact-echo method. Cem. Concr. Res. **31**(10), 1427–1436 (2001). https://doi.org/10.1016/S0008-8846(01)00569-5
39. Scherr, J.F., Große, C.U.: Delamination detection on a concrete bridge deck using impact echo scanning. Struct. Concr. **22**(2), 806–812 (2021). https://doi.org/10.1002/suco.202000415
40. Dai, X., Zhu, J., Tsai, Y.-T., Haberman, M.R.: Use of parabolic reflector to amplify in-air signals generated during impact-echo testing. J. Acoust. Soc. Am. **130**(4), 167–172 (2011). https://doi.org/10.1121/1.3632106
41. Abraham, O., Piwakowski, B., Villain, G., Durand, O.: Non-contact, automated surface wave measurements for the mechanical characterisation of concrete. Constr. Build. Mater. **37**, 904–915 (2012). https://doi.org/10.1016/j.conbuildmat.2012.03.015
42. Gucunski, N., Romero, F., Kruschwitz, S., Feldmann, R., Abu-Hawash, A., Dunn, M.: Multiple complementary nondestructive

evaluation technologies for condition assessment of concrete bridge decks. Transp. Res. Rec. J. Transp. Res. Board **2201**(1), 34–44 (2010). https://doi.org/10.3141/2201-05
43. Schubert, F., Wiggenhauser, H., Lausch, R.: On the accuracy of thickness measurements in impact-echo testing of finite concrete specimens - numerical and experimental results. Ultrasonics **42**(1–9), 897–901 (2004). https://doi.org/10.1016/j.ultras.2004.01.076
44. Guthrie, W.S., Larsen, J.L., Baxter, J.S., Mazzeo, B.A.: Automated air-coupled impact-echo testing of a concrete bridge deck from a continuously moving platform. J. Nondestruct. Eval. **38:32**(1), 1–8 (2019). https://doi.org/10.1007/s10921-019-0566-9
45. Tofeldt, O., Ryden, N.: Lamb wave phase velocity imaging of concrete plates with 2D arrays. J. Nondestruct. Eval. **37**(1), 4 (2018). https://doi.org/10.1007/s10921-017-0457-x
46. Nowotarski, P., Dubas, S., Milwicz, R.: Review of the air-coupled impact-echo method for non-destructive testing. In: IOP Conference Series: Materials Science and Engineering, vol. 245, p. 032098 (2017). https://doi.org/10.1088/1757-899x/245/3/032098 . IOP Publishing
47. Shokouhi, P.: Comprehensive evaluation of concrete bridge decks using impact echo. Ph.d. thesis, Rutgers University, New Jersey (2005)
48. ASTM International: Standard test method for measuring the p-wave speed and the thickness of concrete plates using the impact-echo method. C1383-15 (2022)
49. DGZfP-Fachausschuss für Zerstörungsfreie Prüfung im Bauwesen: Merkblatt B 11: Merkblatt über die Anwendung des Impakt-Echo-Verfahrens zur Zerstörungsfreien Prüfung von Betonbauteilen. Deutsche Gesellschaft für Zerstörungsfreie Prüfung e.V, Technical report (2021)
50. Mazzeo, B.A., Patil, A.N., Guthrie, W.S.: Acoustic impact-echo investigation of concrete delaminations using liquid droplet excitation. NDT & E Int. **51**, 41–44 (2012). https://doi.org/10.1016/j.ndteint.2012.05.007
51. Mazzeo, B.A., Patil, A.N., Hurd, R.C., Klis, J.M., Truscott, T.T., Guthrie, W.S.: Air-coupled impact-echo delamination detection in concrete using spheres of ice for excitation. J. Nondestruct. Eval. **33**(3), 317–326 (2014). https://doi.org/10.1007/s10921-013-0215-7
52. Mori, K., Tokuomi, S.: A new remote non-destructive testing method for concrete structures using water jet impact. In: Proceedings of the 4th World Congress on Civil, Structural, and Environmental Engineering (2019). https://doi.org/10.11159/icsect19.114
53. Scherr, J.F., Kollofrath, J., Popovics, J.S., Bühling, B., Grosse, C.U.: Detection of delaminations in concrete plates using a laser ablation impact echo technique. J. Nondestruct. Eval. **42**(11), 1–13 (2023). https://doi.org/10.1007/s10921-022-00921-x
54. Mori, K., Spagnoli, A., Murakami, Y., Kondo, G., Torigoe, I.: A new non-contacting non-destructive testing method for defect detection in concrete. NDT & E Int. **35**(6), 399–406 (2002). https://doi.org/10.1016/S0963-8695(02)00009-9
55. Dai, X., Zhu, J., Haberman, M.R.: A focused electric spark source for non-contact stress wave excitation in solids. J. Acoust. Soc. Am. **134**(6), 513–519 (2013). https://doi.org/10.1121/1.4826913
56. Lamb, H.: On waves in an elastic plate. Proc. R. Soc. London. Series A **93**(648), 114–128 (1917). https://doi.org/10.1098/rspa.1917.0008
57. Schubert, F., Köhler, B.: Ten lectures on impact-echo. J. Nondestruct. Eval. **27**(1–3), 5–21 (2008). https://doi.org/10.1007/s10921-008-0036-2
58. Holland, S.D., Chimenti, D.E.: High contrast air-coupled acoustic imaging with zero group velocity Lamb modes. Ultrasonics **42**(1–9), 957–960 (2004). https://doi.org/10.1016/j.ultras.2003.12.009
59. Holland, S.D., Chimenti, D.E.: Air-coupled acoustic imaging with zero-group-velocity Lamb modes. Appl. Phys. Lett. **83**(13), 2704–2706 (2003). https://doi.org/10.1063/1.1613046
60. Gibson, A., Popovics, J.S.: Lamb wave basis for impact-echo method analysis. J. Eng. Mech. **131**(4), 438–443 (2005). https://doi.org/10.1061/(ASCE)0733-9399(2005)131:4(438)
61. Abraham, O., Popovics, J.S.: Impact–echo techniques for evaluation of concrete structures. In: Non-Destructive Evaluation of Reinforced Concrete Structures, pp. 466–489. Elsevier (2010). https://doi.org/10.1533/9781845699604.2.466
62. Garbacz, A., Piotrowski, T., Courard, L., Kwaśniewski, L.: On the evaluation of interface quality in concrete repair system by means of impact-echo signal analysis. Construct. Build. Mater. **134**, 311–323 (2017). https://doi.org/10.1016/j.conbuildmat.2016.12.064
63. Thomson, W.: XLVI. hydrokinetic solutions and observations. Lond. Edinb. Dublin Philos. Magaz J. Sci. **42**(281), 362–377 (1871) https://doi.org/10.1080/14786447108640585
64. Helmholtz, H.: Über Discontinuirliche Flüssigkeits-Bewegungen. Akademie der Wissenschaften zu Berlin (1868)
65. Wygnanski, I., Fiedler, H.E.: The two-dimensional mixing region. J. Fluid Mech. **41**(2), 327–361 (1970). https://doi.org/10.1017/S0022112070000630
66. Tam, C.K.W.: Supersonic jet noise. Ann. Rev. Fluid Mech. **27**(1), 17–43 (1995). https://doi.org/10.1146/annurev.fl.27.010195.000313
67. Lush, P.A.: Measurements of subsonic jet noise and comparison with theory. J. Fluid Mech. **46**(3), 477–500 (1971). https://doi.org/10.1017/S002211207100065X
68. Sondhauss, C.: Ueber die beim Ausströmen der Luft entstehenden Töne. Annalen der Physik **167**(2), 214–240 (1854). https://doi.org/10.1002/andp.18541670204
69. Kearney-Fischer, M., Sinha, A., Samimy, M.: Intermittent nature of subsonic jet noise. AIAA J. **51**(5), 1142–1155 (2013). https://doi.org/10.2514/1.J051930
70. Raman, G.: Supersonic jet screech: half-century from Powell to the present. J. Sound Vib. **225**(3), 543–571 (1999). https://doi.org/10.1006/jsvi.1999.2181
71. Rolls-Royce.: The Jet Engine. John Wiley & Sons, USA (2015)
72. Morris, P.J., Viswanathan, K.: Jet Noise. Springer, Germany (2013). https://doi.org/10.1007/978-3-7091-1458-2
73. Norum, T.D.: Screech suppression in supersonic jets. AIAA J. **21**(2), 235–240 (1983). https://doi.org/10.2514/3.8059
74. Powell, A.: On the mechanism of choked jet noise. Proc. Phys. Soc. Sect. B **66**(12), 1039 (1953). https://doi.org/10.1088/0370-1301/66/12/306
75. Raman, G.: Advances in understanding supersonic jet screech: review and perspective. Progr. Aerospace Sci. **34**(1–2), 45–106 (1998). https://doi.org/10.1016/S0376-0421(98)00002-5
76. Sinibaldi, G., Lacagnina, G., Marino, L., Romano, G.P.: Aeroacoustics and aerodynamics of impinging supersonic jets: Analysis of the screech tones. Phys. Fluids **25**(8), 086104 (2013). https://doi.org/10.1063/1.4819333
77. Edgington-Mitchell, D.: Aeroacoustic resonance and self-excitation in screeching and impinging supersonic jets - A review. Int. J. Aeroacoust. **18**(2–3), 1–71 (2019). https://doi.org/10.1177/1475472X19834521
78. Brown, G.L., Roshko, A.: On density effects and large structure in turbulent mixing layers. J. Fluid Mech. **64**(4), 775–816 (1974). https://doi.org/10.1017/S002211207400190X
79. Hussain, A.K.M.F., Reynolds, W.C.: The mechanics of an organized wave in turbulent shear flow. J. Fluid Mech. **41**(2), 241–258 (1970). https://doi.org/10.1017/S0022112070000605
80. Oberleithner, K., Rukes, L., Soria, J.: Mean flow stability analysis of oscillating jet experiments. J. Fluid Mech. **757**, 1–32 (2014). https://doi.org/10.1017/jfm.2014.472

81. Krothapalli, A., Rajkuperan, E., Alvi, F., Lourenco, L.: Flow field and noise characteristics of a supersonic impinging jet. J. Fluid Mech. **392**, 155–181 (1999). https://doi.org/10.1017/S0022112099005406
82. Henderson, B.: The connection between sound production and jet structure of the supersonic impinging jet. J. Acoust. Soc. Am. **111**(2), 735–747 (2002). https://doi.org/10.1121/1.1436069
83. Henderson, B., Bridges, J., Wernet, M.: An experimental study of the oscillatory flow structure of tone-producing supersonic impinging jets. J. Fluid Mech. **542**, 115–137 (2005). https://doi.org/10.1017/S0022112005006385
84. Umeda, Y., Ishii, R.: On the sound sources of screech tones radiated from choked circular jets. J. Acoust. Soc. Am. **110**(4), 1845–1858 (2001). https://doi.org/10.1121/1.1402620
85. Dhamanekar, A., Srinivasan, K.: Effect of impingement surface roughness on the noise from impinging jets. Phys. Fluids **26**(3), 036101 (2014). https://doi.org/10.1063/1.4866977
86. Brehm, C., Housman, J.A., Kiris, C.C.: Noise generation mechanisms for a supersonic jet impinging on an inclined plate. J. Fluid Mech. **797**, 802–850 (2016). https://doi.org/10.1017/jfm.2016.244
87. Tam, C.K.W., Auriault, L.: Mean flow refraction effects on sound radiated from localized sources in a jet. J. Fluid Mech. **370**, 149–174 (1998). https://doi.org/10.1017/S0022112098001852
88. Bühling, B., Strangfeld, C., Maack, S., Schweitzer, T.: Experimental analysis of the acoustic field of an ultrasonic pulse induced by a fluidic switch. J. Acoust. Soc. Am. **149**(4), 2150–2158 (2021). https://doi.org/10.1121/10.0003937
89. Choi, D.W., McIntyre, C., Hutchins, D.A., Billson, D.R.: Gas jet as a waveguide for air-coupled ultrasound. Ultrasonics **40**(1–8), 145–151 (2002). https://doi.org/10.1016/S0041-624X(02)00128-2
90. Bühling, B., Maack, S., Schweitzer, T., Strangfeld, C.: Enhancing the spectral signatures of ultrasonic fluidic transducer pulses for improved time-of-flight measurements. Ultrasonics **119**, 106612 (2022). https://doi.org/10.1016/j.ultras.2021.106612
91. Bühling, B., Küttenbaum, S., Maack, S., Strangfeld, C.: Development of an accurate and robust air-coupled ultrasonic time-of-flight measurement technique. Sensors **22**(2135), 1–17 (2022). https://doi.org/10.3390/s22062135
92. Grotelüschen, B., Bühling, B.: Impact-Echo Dataset "IE Platte". https://doi.org/10.7910/DVN/EH4E9G
93. Aßmann, N., Bühling, B.: Impact-Echo Dataset "Radarplatte". https://doi.org/10.7910/DVN/UNOH2U
94. Niederleithinger, E., Gardner, S., Kind, T., Kaiser, R., Grunwald, M., Yang, G., Redmer, B., Waske, A., Mielentz, F., Effner, U., et al.: Muon tomography of the interior of a reinforced concrete block: First experimental proof of concept. J. Nondestruct. Eval. **40**(3), 1–14 (2021). https://doi.org/10.1007/s10921-021-00797-3

Authors and Affiliations

Christoph Strangfeld[1] · Bjarne Grotelüschen[1] · Benjamin Bühling[2]

✉ Christoph Strangfeld
christoph.strangfeld@bam.de

Bjarne Grotelüschen
bjarne.grotelueschen@bam.de

Benjamin Bühling
benjamin.buehling@bam.de

[1] Department 8: Non-destructive Testing, Bundesanstalt für Materialforschung und -prüfung, Unter den Eichen 87, Berlin 12205, Germany

[2] Department 3: Containment Systems for Dangerous Goods; Energy Storage, Berlin 12205, Germany